

# Constraining the core radius and density jumps inside Earth using atmospheric neutrino oscillations

---

**Anuj Kumar Upadhyay,<sup>a,b</sup> Anil Kumar,<sup>b,c,d</sup> Sanjib Kumar Agarwalla,<sup>b,d,e</sup> Amol Dighe<sup>f</sup>**

<sup>a</sup>*Department of Physics, Aligarh Muslim University, Aligarh-202002, India*

<sup>b</sup>*Institute of Physics, Sachivalaya Marg, Sainik School Post, Bhubaneswar 751005, India*

<sup>c</sup>*Applied Nuclear Physics Division, Saha Institute of Nuclear Physics, Block AF, Sector 1, Bidhannagar, Kolkata 700064, India*

<sup>d</sup>*Homi Bhabha National Institute, Anushakti Nagar, Mumbai 400094, India*

<sup>e</sup>*Department of Physics & Wisconsin IceCube Particle Astrophysics Center, University of Wisconsin, Madison, WI 53706, U.S.A*

<sup>f</sup>*Tata Institute of Fundamental Research, Homi Bhabha Road, Colaba, Mumbai 400005, India*

*E-mail:* [anuju@iopb.res.in](mailto:anuju@iopb.res.in) (ORCID: 0000-0003-1957-2626),  
[anil.k@iopb.res.in](mailto:anil.k@iopb.res.in) (ORCID: 0000-0002-8367-8401), [sanjib@iopb.res.in](mailto:sanjib@iopb.res.in)  
(ORCID: 0000-0002-9714-8866), [amol@theory.tifr.res.in](mailto:amol@theory.tifr.res.in) (ORCID:  
0000-0001-6639-0951)

**ABSTRACT:** Atmospheric neutrinos can act as a tool to probe the interior of Earth using weak interactions, and can provide information complementary to that obtained from gravitational and seismic measurements. While passing through Earth, multi-GeV neutrinos encounter Earth matter effects due to the coherent forward scattering with the ambient electrons, which alter the neutrino oscillation probabilities. These matter effects depend upon the density distribution of electrons inside Earth, and hence, can be used to determine the internal structure of Earth. In this work, we employ a five-layered model of Earth where the layer densities and radii are modified, keeping the mass and moment of inertia of Earth unchanged and respecting the hydrostatic equilibrium condition. We use the proposed INO-ICAL detector as an example of an atmospheric neutrino experiment that can distinguish between neutrinos and antineutrinos efficiently in the multi-GeV energy range. Our analysis demonstrates the role such an experiment can play in simultaneously constraining the density jumps inside Earth and the location of the core-mantle boundary.

**KEYWORDS:** Earth Tomography, Atmospheric Neutrinos, Neutrino Oscillations, Matter Effect, ICAL, INO

ARXIV EPRINT: [2405.xxxxx](https://arxiv.org/abs/2405.xxxxx)

---

## Contents

<b>1</b>	<b>Introduction</b>	<b>1</b>
<b>2</b>	<b>Neutrino oscillations with density jumps and location of CMB</b>	<b>4</b>
2.1	Five-layered models with modified density jumps and location of CMB	4
2.2	Effects of modified density jumps and location of CMB on oscillation probabilities	8
2.3	Effect of modified density jumps and location of CMB on oscillograms	10
<b>3</b>	<b>Atmospheric neutrinos at INO-ICAL</b>	<b>13</b>
<b>4</b>	<b>Numerical analysis</b>	<b>16</b>
<b>5</b>	<b>Results</b>	<b>17</b>
5.1	Constraining correlated density jumps assuming the standard CMB location	17
5.2	Constraining correlated density jumps and location of CMB	20
5.3	Impact of different true choices of $\sin^2 \theta_{23}$	20
<b>6</b>	<b>Summary and conclusions</b>	<b>23</b>

---

## 1 Introduction

The knowledge of the internal structure of Earth is important not only for understanding the effects of its dynamics on the surface, but also as an input for reconstructing the formation and geological evolution of Earth. The information on the internal structure and chemical composition of Earth are difficult to obtain due to the large temperature, pressure, and extreme environments. Most of the information about the internal structure of Earth comes from the indirect methods, mainly gravitational measurements [1–6] and seismic studies [7–16].

The gravitational measurements provide the values of the mass of Earth,  $M_E = (5.9722 \pm 0.0006) \times 10^{24}$  kg [1–5], and its moment of inertia,  $I_E = (8.01736 \pm 0.00097) \times 10^{37}$  kg·m<sup>2</sup> [5, 6]. These measurements already indicate that the density of Earth cannot be uniform everywhere inside; rather, the density closer to the center of Earth should be larger. This maybe inferred from the following. A uniform sphere of mass  $M_E$  and radius  $R_E = 6371$  km would have a moment of inertia  $I_E = (2/5)M_ER_E^2 = 9.7 \times 10^{37}$  kg·m<sup>2</sup>, which is significantly more than the experimentally measured value of  $I_E$ . Also, the average density of Earth obtained from  $M_E$  and the radius  $R_E$ , i.e.,  $\rho_{\text{avg}} \sim 5.5$  g/cm<sup>3</sup>, is larger than the density of rocks on the surface,  $\rho \sim 2.8$  g/cm<sup>3</sup>. Both of these observations are consistent with a high density region present deep inside Earth.

The details of this increase in density as we go deeper inside Earth maybe discerned from seismological measurements. Seismic waves originate from their epicenters, which typically lie at a depth of up to 700 km [9, 12]. These are mechanical waves which propagate through different regions inside Earth, and their velocities modify depending upon the properties of the media they traverse. They can reflect or refract when they encounter changes in densities, pressures, and physical properties of the medium. The seismic studies indicate that Earth has a layered structure in the form of concentric spherical shells. The layers inside Earth can be mainly classified into crust, outer mantle, inner mantle, outer core and inner core, where the density increases as we go deeper inside towards the inner core. This increase in density is not always gradual; there are sharp density changes at the transition regions between any two of the layers. The sharpest such transition is observed while going from the inner mantle to the outer core; this core-mantle boundary (CMB) is located around  $R_{\text{CMB}} = 3483 \pm 5$  km [7, 17].

The seismic activities can give rise to body waves, surface waves, and normal modes or free waves. The body waves can be further classified into two categories – pressure (P) and shear (S) waves. The P-waves can propagate through both solid as well as liquid medium. On the other hand, the S-waves can only travel through solid medium. Since S-waves cannot travel through outer core and the velocity of P-waves decreases there, the outer core is inferred to be liquid [8]. In 1936, the inner core was discovered by I. Lehmann owing to the observation of higher velocity of P-waves therein [18]. Unlike outer core, the inner core is believed to be solid in nature [19]. The surface waves are slower than the body waves and are mainly sensitive to upper mantle, providing information on their velocities. The normal modes or free waves come into the picture when the whole Earth oscillates. They are sensitive to the large structure inside Earth providing information on their velocities and densities of the ambient matter.

The density distribution inside Earth is obtained by the nonlinear inversion of velocity distributions of the seismic waves. This indirect technique is used to develop Earth density models [20–25]; one of the well-known models is the Preliminary Reference Earth Model (PREM) [26]. Furthermore, the waves velocities depend upon temperature, pressure, composition, and elastic properties of the layers of Earth, which give rise to uncertainties in the determination of the density distribution. The density of the mantle is uncertain about 5%, whereas the core is the most uncertain region of Earth [27–29].

Even though the huge amount of data from seismic studies and gravitational measurements have significantly improved our understanding of the internal structure of Earth, we still have many open issues. For example, the mass, radius, and chemical composition of core still have uncertainties. The density jump while going from outer core to inner core is not well-known. We do not know how much light element like H is present inside the core [15, 30, 31]. The measurement of power produced during radioactive decay inside core and mantle could help us understand the thermal dynamics [32–35]. Therefore, complementary and independent probes such as geoneutrino detection [32, 34, 36–39], neutrino absorption [40–42], and neutrino oscillations [43] could further improve our understanding about the interiors of Earth.

Neutrinos are an appealing tool for providing an independent pathway to learn about

the interior of Earth via their weak interactions with matter, which is complementary to the electromagnetic interactions of seismic studies and gravitational interactions. The idea of exploiting the attenuation of neutrinos at energies above a few TeV [44, 45] to learn about the Earth’s interior was first suggested in Refs. [46, 47]. The detailed studies using various neutrino sources, such as man-made neutrinos [40, 46–60], extraterrestrial neutrinos [54, 61–64], and atmospheric neutrinos [41, 42, 65–67], have also been carried out. On the other hand, the discovery of a non-zero value of reactor mixing angle  $\theta_{13}$ , and precise measurement of other neutrino oscillation parameters [68–71] have provided an independent probe to the Earth’s interior using matter effects in neutrino oscillations at energies of about a few GeV. This possibility is called “neutrino oscillation tomography”, and has been studied using man-made neutrino beams [72–82], solar neutrinos [83–89], supernova neutrinos [85, 90, 91], and atmospheric neutrinos [43, 92–107].

Atmospheric neutrinos are the best source of neutrinos for performing Earth tomography because they have energies covering the multi-GeV range where Earth matter effects are significant, and wide range of baselines starting from  $\sim 15$  km to 12757 km. The neutrinos passing through mantle experience the Mikheyev-Smirnov-Wolfenstein (MSW) resonance [108–110] in the energy range of 6 to 10 GeV. On the other hand, the core-passing neutrinos with energies of 3 – 6 GeV experience another kind of resonance which is known as neutrino oscillation length resonance (NOLR) [111–115] or parametric resonance (PR) [116, 117]. The efficient observations of these matter effects resonances could help us in probing the physical and chemical properties of core and mantle regions inside Earth. Using matter effects in the atmospheric neutrino oscillations, numerous sensitivity studies have been performed recently for current and future experiments like IceCube [118], DeepCore [118, 119], Precision IceCube Next Generation Upgrade (PINGU) [93], Oscillation Research with Cosmics in the Abyss (ORCA) [120], Deep Underground Neutrino Experiment (DUNE) [121], Hyper-Kamiokande (Hyper-K) [122], and Iron Calorimeter (ICAL) [123] detector. These studies include validating the core-mantle boundary (CMB) using ICAL [99, 124], determining the position of the core-mantle boundary using DUNE [101] and ICAL [106, 124, 125], determining the average densities of the core and the mantle using ORCA [43, 100, 103] and DUNE [102], probing the possible presence of dark matter inside Earth using ICAL [107, 124], and exploring the chemical composition of the Earth’s core using PINGU [93], Hyper-K and IceCube [94], and ORCA [95–97, 100, 104, 105]. The prospects of establishing the Earth’s matter effect, validating the non-homogeneous density profile inside Earth, and measuring the mass of Earth and its core using oscillation of weakly interacting neutrino at GeV energies in the context of DeepCore are shown in Ref. [126].

Detectors that can distinguish neutrinos from antineutrinos have a special role to play in this exploration, since they may be able to cleanly observe the MSW as well as NOLR/PR resonances without any dilution. Therefore, we focus on the proposed magnetized Iron Calorimeter (ICAL) detector at the India-based Neutrino Observatory (INO) [123]. This detector is optimized to detect multi-GeV atmospheric neutrinos and antineutrinos separately. Owing to its excellent angular resolution, it would be able to observe the neutrinos passing through the core and mantle. The good energy resolution would enable ICAL to

efficiently observe MSW and NOLR/PR resonances of matter effects. These resonances depend on the matter densities of the layers inside Earth and the location of layer boundaries. Thanks to these features, ICAL would be sensitive to the amount of density jump at the layer boundaries and the location of CMB. In Ref. [99], some of the present authors had calculated the expected sensitivity of the ICAL detector to determine the presence of a core-mantle boundary with a given density jump and a given position of CMB. As a followup work in Ref. [106], we evaluated the expected sensitivity of the ICAL detector to locate the position of the CMB, assuming various cases.

In the present work, we quantify the statistical significance of the ICAL detector to measure the density jumps at various boundaries and the location of CMB radius simultaneously. We take into account the constraints from the mass of Earth, the moment of inertia of Earth, and the hydrodynamic condition of increasing density with decreasing radius. We demonstrate that a five-layered model is sufficient to incorporate these constraints and perform a 2D analysis in the parameter space of the CMB radius and one of the density jumps. We also present the expected sensitivities for individual density jumps when the CMB radius is fixed.

In section 2.1, we describe a five-layered density profile of Earth used in the present analysis and the procedure to modify the density jumps at layer boundaries and the location of CMB while respecting the constraints such as the total mass and the moment of inertia of Earth. The sections 2.2 and 2.3 present the effects of modifications in the density jumps at the layer boundaries and the location of CMB on the neutrino oscillation probabilities. In section 3, we describe the procedure to simulate the reconstructed events at the ICAL detector, and the effects of modified density jumps and CMB location on reconstructed event distributions. The details regarding numerical analysis are mentioned in section 4. We present our results in section 5 where we evaluate the expected sensitivity of ICAL to measure the density jumps at layers boundaries and the CMB location. We also show the impact of different true choices of mixing angle  $\theta_{23}$  on our sensitivities. Finally, we present the summary and conclude in section 6.

## 2 Neutrino oscillations with density jumps and location of CMB

In this section, we explore the effects of variations in the correlated density jumps and the location of the core-mantle boundary ( $R_{\text{CMB}}$ ) on the oscillation probabilities of atmospheric neutrinos. These variations can modify the matter effects of Earth, which in turn can alter the neutrino oscillation probabilities. Now, we describe the model of density distribution inside Earth which we have used to perform the present analysis.

### 2.1 Five-layered models with modified density jumps and location of CMB

In this analysis, we consider a five-layered density profile of Earth<sup>1</sup>, where each layer has a constant density. This density profile is guided by the PREM [26] profile. The five distinct layers are the inner core (IC), the outer core (OC), the inner mantle (IM), the

---

<sup>1</sup>The rationale for a five-layered profile will be clear later in this section.

Five-layered profile	Radii of layers (km)					Layer densities $\rho$ (g/cm <sup>3</sup> )				
	$R_{IC}$	$R_{OC}$	$R_{IM}$	$R_{MM}$	$R_{OM}$	$\rho_{IC}$	$\rho_{OC}$	$\rho_{IM}$	$\rho_{MM}$	$\rho_{OM}$
<b>Standard</b>	1221.5	3480	5701	6151	6371	13.5	11.0	5.0	3.6	2.75
<b>1D-modifications</b>										
Smaller jump (SJ)	1221.5	3480	5701	6151	6371	12.64	10.3	5.48	2.77	2.75
Larger jump (LJ)	1221.5	3480	5701	6151	6371	14.36	11.7	4.52	4.42	2.75
<b>2D-modifications</b>										
Smaller jump at larger core (SJLC)	1221.5	3980	5701	6151	6371	11.29	9.2	5.22	2.79	2.75
Larger jump at smaller core (LJSC)	1221.5	2980	5701	6151	6371	18.16	14.8	4.65	4.59	2.75

**Table 1:** The outer radii of layers and the densities of layers in the five-layered profile of Earth for the representative choices shown in Fig. 1. For 1D-modifications, only  $\Delta\rho_{CMB}$  is modified while  $R_{CMB}$  is kept fixed at the standard value. The smaller jump (SJ) scenario corresponds to  $\Delta\rho_{CMB}$  of 4.82 g/cm<sup>3</sup>, whereas the larger jump (LJ) scenario corresponds to  $\Delta\rho_{CMB}$  of 7.18 g/cm<sup>3</sup>. For 2D-modifications, both  $\Delta\rho_{CMB}$  and  $R_{CMB}$  are modified. The smaller jump at a larger core (SJLC) scenario represents  $\Delta\rho_{CMB}$  of 3.98 g/cm<sup>3</sup> for a given  $\Delta R_{CMB} = +500$  km, whereas the larger jump at a smaller core (LJSC) scenario represents  $\Delta\rho_{CMB}$  of 10.15 g/cm<sup>3</sup> for  $\Delta R_{CMB} = -500$  km. The total mass and moment of inertia of Earth have been kept unchanged during these modifications.

middle mantle (MM), and the outer mantle (OM), with respective densities denoted by  $\rho_{IC}$ ,  $\rho_{OC}$ ,  $\rho_{IM}$ ,  $\rho_{MM}$ , and  $\rho_{OM}$ . Here, we do not consider the crust because of the relatively smaller thickness. In this five-layered model, the four significant density jumps occur at the following boundaries:

- the inner core - outer core boundary with radius  $R_{IC}$  and density jump  $\Delta\rho_{IC-OC} = \rho_{IC} - \rho_{OC}$ ,
- the outer core - inner mantle boundary, also known as CMB, with radius  $R_{CMB}$  (or  $R_{OC}$ ) and density jump  $\Delta\rho_{CMB} = \rho_{OC} - \rho_{IM}$ ,
- the inner mantle - middle mantle boundary with radius  $R_{IM}$  and density jump  $\Delta\rho_{IM-MM} = \rho_{IM} - \rho_{MM}$ ,
- the middle mantle - outer mantle boundary with radius  $R_{MM}$  and density jump  $\Delta\rho_{MM-OM} = \rho_{MM} - \rho_{OM}$ .

The outer mantle is bounded by the radius of Earth  $R_E$ . The standard values of the density and radius for each of these layers are given in the first row of Table 1.

In the five-layered model, the total mass ( $M_E$ ) and moment of inertia ( $I_E$ ) of Earth

are given by

$$M_E = \frac{4\pi}{3} \left[ \rho_{IC} R_{IC}^3 + \rho_{OC} (R_{CMB}^3 - R_{IC}^3) + \rho_{IM} (R_{IM}^3 - R_{CMB}^3) + \rho_{MM} (R_{MM}^3 - R_{IM}^3) + \rho_{OM} (R_E^3 - R_{MM}^3) \right], \quad (2.1)$$

$$I_E = \frac{8\pi}{15} \left[ \rho_{IC} R_{IC}^5 + \rho_{OC} (R_{CMB}^5 - R_{IC}^5) + \rho_{IM} (R_{IM}^5 - R_{CMB}^5) + \rho_{MM} (R_{MM}^5 - R_{IM}^5) + \rho_{OM} (R_E^5 - R_{MM}^5) \right]. \quad (2.2)$$

$M_E$  and  $I_E$  can be also written in terms of the density jumps at the layer boundaries ( $\Delta\rho_{IC-OC}$ ,  $\Delta\rho_{OC-IM}$ ,  $\Delta\rho_{IM-MM}$ , and  $\Delta\rho_{MM-OM}$ ):

$$M_E = \frac{4\pi}{3} \left[ \Delta\rho_{IC-OC} R_{IC}^3 + \Delta\rho_{OC-IM} R_{CMB}^3 + \Delta\rho_{IM-MM} R_{IM}^3 + \Delta\rho_{MM-OM} R_{MM}^3 + \rho_{OM} R_E^3 \right], \quad (2.3)$$

$$I_E = \frac{8\pi}{15} \left[ \Delta\rho_{IC-OC} R_{IC}^5 + \Delta\rho_{OC-IM} R_{CMB}^5 + \Delta\rho_{IM-MM} R_{IM}^5 + \Delta\rho_{MM-OM} R_{MM}^5 + \rho_{OM} R_E^5 \right]. \quad (2.4)$$

Equations 2.3 and 2.4 have total ten parameters corresponding to the five density jumps and five radii at the layer boundaries. We consider the following constraints:

- The total mass  $M_E = 5.972 \times 10^{24}$  kg and moment of inertia  $I_E = 8.017 \times 10^{37}$  kg·m<sup>2</sup> of Earth are taken to be fixed.
- Since the density of the outer mantle is very well-known,  $\rho_{OM}$  is taken to be fixed at  $\rho_{OM} = 2.75$  g/cm<sup>3</sup>.
- The radius of Earth has been taken to be  $R_E = 6371$  km. The radii of the inner mantle and the middle mantle are fixed at  $R_{IM} = 5701$  km and  $R_{MM} = 6151$  km, respectively.

Note that the above constraints are written in the decreasing order of strictness. Thus, we have a total of 6 constraints and we are left with 4 free parameters, all related to the core, which we choose to be  $R_{CMB}$ ,  $\Delta\rho_{CMB}$ ,  $R_{IC}$ , and  $\rho_{IC}/\rho_{OC}$ . Since we would like to focus on the sensitivity to  $R_{CMB}$  and  $\Delta\rho_{CMB}$  in this paper, we keep  $R_{IC} = 1221.5$  km and  $\rho_{IC}/\rho_{OC} = 1.227$  fixed in our analysis. These values are close to the values in the standard PREM profile.

All the above constraints have the form of equalities. We also impose an additional constraint that has the form of an inequality. This is the hydrostatic equilibrium condition where the density of the inner layer is always greater than that of the outer layer ( $\rho_{\text{inner layer}} > \rho_{\text{outer layer}}$ ). This constraint does not affect the number of degrees of freedom, which stays at two, viz.  $R_{CMB}$  and  $\Delta\rho_{CMB}$ .

The procedure we adopt for incorporating the above constraints is as follows. First, we solve Eqs. 2.1 and 2.2 in terms of the two independent parameters<sup>2</sup>  $R_{\text{CMB}}$  and  $\Delta\rho_{\text{CMB}}$ . In the upcoming sections, we study the effects of the modifications of these two parameters on neutrino oscillation probabilities for the following two cases:

- 1-dimensional (1D) modification:  $R_{\text{CMB}}$  is fixed at 3480 km and only  $\Delta\rho_{\text{CMB}}$  is varied
- 2-dimensional (2D) modification:  $R_{\text{CMB}}$  is varied simultaneously with  $\Delta\rho_{\text{CMB}}$ .

A 1D modification for  $R_{\text{CMB}}$  is also possible where  $\Delta\rho_{\text{CMB}}$  is kept fixed. However, this modification has already been explored in Ref. [106] where the authors estimated the sensitivity to measure the location of CMB ( $R_{\text{CMB}}$ ) using a three-layered profile.

We would like to highlight the fact that the density profile of Earth should have at least five layers if we want to explore the correlated effects of  $R_{\text{CMB}}$  and  $\Delta\rho_{\text{CMB}}$  while respecting the above-mentioned eight constraints. At the same time, a five-layered profile is sufficient to capture all the relevant features of the three-flavor neutrino oscillation probability in the presence of matter. The profile with more number of layers do not change neutrino oscillation probabilities significantly. Therefore, in the present work, we use the five-layered density profile of Earth which is guided by the PREM profile.

Table 1 shows some benchmark values of the 1D modifications, which correspond to the following two scenarios:

- SJ: a smaller jump of  $\Delta\rho_{\text{CMB}} = 4.82 \text{ g/cm}^3$ ,
- LJ: a larger jump of  $\Delta\rho_{\text{CMB}} = 7.18 \text{ g/cm}^3$ ,

at the standard CMB where  $R_{\text{CMB}}$  is kept fixed at 3480 km. Note that these benchmark values correspond to the maximum possible modifications in  $\Delta\rho_{\text{CMB}}$  for the corresponding  $R_{\text{CMB}}$ , taking into account the above-mentioned eight constraints. The density distributions for profiles with standard jump (black curve), SJ (dashed-blue curve), and LJ (dotted-red curve) are shown in the left panel of Fig. 1.

The benchmark values of the 2D modifications in Table 1 correspond to the following two scenarios:

- SJLC: a smaller jump,  $\Delta\rho_{\text{CMB}} = 3.98 \text{ g/cm}^3$ , at a larger core,  $\Delta R_{\text{CMB}} = +500 \text{ km}$ ,
- LJSC: a larger jump,  $\Delta\rho_{\text{CMB}} = 10.15 \text{ g/cm}^3$ , at a smaller core,  $\Delta R_{\text{CMB}} = -500 \text{ km}$ .

The right panel of Fig. 1 shows the density distributions for profiles with standard jump at standard CMB (black curve), SJLC (dashed-blue curve), and LJSC (dotted-red curve). Now, we discuss the effects of the modifications of the density jump at CMB and the location of CMB on neutrino oscillation probabilities in the next section.

---

<sup>2</sup>Note that one of the other density jumps like  $\Delta\rho_{\text{IC-OC}}$ ,  $\Delta\rho_{\text{IM-MM}}$  and  $\Delta\rho_{\text{MM-OM}}$ , can also be chosen as the second independent parameter. In our result section, we will also interpret our sensitivities in terms of these density jumps.

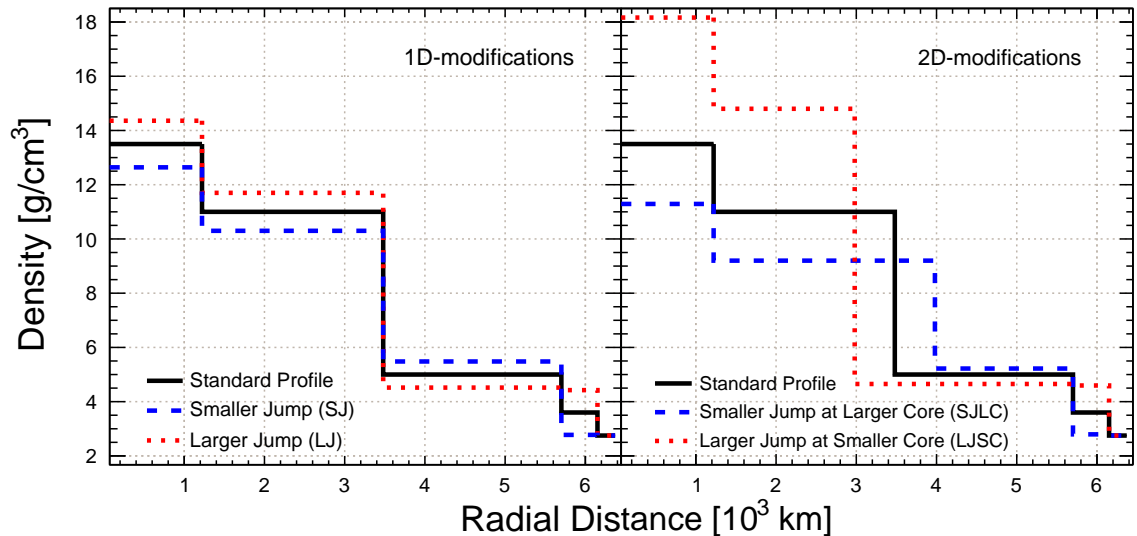


**Figure 1:** The five-layered density profiles of Earth as functions of the radial distances for some representative choices of density jumps at the location of CMB as mentioned in Table 1. The black curves correspond to the standard density profile (the first row in Table 1) with a density jump of  $\Delta\rho_{\text{CMB}} = 6.0 \text{ g/cm}^3$  at CMB with its standard location of  $R_{\text{CMB}} = 3480 \text{ km}$ . The left panel presents the 1D-modifications, where dashed-blue (dotted-red) curve represents the SJ (LJ) scenario with the standard CMB as mentioned in the Table 1. The right panel corresponds to the 2D-modifications, where dashed-blue (dotted-red) curve denotes the SJLC (LJSC) scenario as mentioned in the Table 1.

## 2.2 Effects of modified density jumps and location of CMB on oscillation probabilities

Atmospheric neutrinos and antineutrinos are produced about 15 km above the surface of Earth. They possess a wide range of energies from sub-GeV to a few TeV and travel over baselines ranging from about 15 km to 12757 km. While passing through Earth, the upward-going multi-GeV neutrinos encounter the Earth’s matter effects due to the charged-current (CC) interactions with the ambient electrons. The effective matter potential is given by

$$V_{\text{CC}} = \pm \sqrt{2} G_F N_e \approx \pm 7.6 \times Y_e \times 10^{-14} \left[ \frac{\rho}{\text{g/cm}^3} \right] \text{ eV}, \quad (2.5)$$

where  $N_e$  is the ambient electron number density,  $G_F$  is the Fermi coupling constant, and  $Y_e = N_e / (N_p + N_n)$  is the electron fraction inside the matter having mass density  $\rho$ . Here,  $N_p$  and  $N_n$  denote the number densities of protons and neutrons inside matter. In our analysis, we consider  $Y_e = 0.466$  for IC and OC (corresponding to a pure FeNi core) and  $Y_e = 0.494$  for IM, MM, and OM (corresponding to a pyrolite mantle) as proposed in Ref. [94]. The  $\pm$  signs correspond to neutrinos and antineutrinos, respectively. Due to these opposite signs for  $V_{\text{CC}}$ , oscillation probabilities for neutrinos and antineutrinos modify differently inside matter. Thanks to the charge identification capability of the ICAL detector, it would be able to observe these different matter effects in neutrinos and antineutrinos separately,

$\sin^2 2\theta_{12}$	$\sin^2 \theta_{23}$	$\sin^2 2\theta_{13}$	$\Delta m_{\text{eff}}^2$ (eV <sup>2</sup> )	$\Delta m_{21}^2$ (eV <sup>2</sup> )	$\delta_{\text{CP}}$	Mass Ordering
0.855	0.5	0.0875	$2.49 \times 10^{-3}$	$7.4 \times 10^{-5}$	0	Normal (NO)

**Table 2:** The benchmark values of neutrino oscillation parameters considered in this work. These values are consistent with the present global fits [68–71] to the neutrino data.

which is expected to enhance the sensitivity of ICAL for physics driven by matter effects. In this work, we perform the analysis using the benchmark values of oscillation parameters given in Table 2. Since we evaluate the sensitivities using 20 years of exposure, at this time scale, these parameters, along with the mass ordering, are expected to be measured precisely [127]. Therefore, the values of these parameters are kept fixed, and the normal mass ordering (NO) is considered during the analysis.

The matter potential modifies the effective masses and flavor mixing of neutrinos [108–110]. As a result, it alters oscillation probabilities of neutrinos passing through Earth. The resonant enhancement of neutrino oscillation probabilities due to the matter effects is known as the Mikheyev-Smirnov-Wolfenstein (MSW) resonance [108–110]. The MSW resonance is significant in neutrinos for normal mass ordering (NO),  $m_1 < m_2 < m_3$ , and in antineutrinos for inverted mass ordering (IO),  $m_3 < m_1 < m_2$ . The MSW resonance depends upon the neutrino energy and the ambient electron density. In particular, the neutrinos passing through the mantle feel the MSW resonance at energies of about 6 – 10 GeV. In addition, the core-passing neutrinos propagate through a sharp jump in density between the mantle and core at CMB, which leads to significant changes in the oscillation probabilities at energies of about 3 – 6 GeV. This phenomenon is known as the neutrino oscillation length resonance (NOLR) [111–115] or parametric resonance (PR) [116, 117]. The NOLR/ PR resonance also depends upon the density jump at CMB and its location. In this work, we study the effect of modification in the density jump at CMB and its location on the neutrino oscillation probabilities.

ICAL would be mainly sensitive to muon-type neutrino events, which are contributed by both  $\nu_\mu \rightarrow \nu_\mu$  disappearance channel and  $\nu_e \rightarrow \nu_\mu$  appearance channel. However, more than 98% of the contribution to  $\nu_\mu$  would come from the disappearance channel. Therefore, we present the effects of modifications in density jump at CMB and its location only for  $\nu_\mu \rightarrow \nu_\mu$  disappearance channel. Figure 2 shows the three-flavor  $\nu_\mu \rightarrow \nu_\mu$  survival probability as a function of neutrino energy for NO. We consider a baseline of 12000 km, which allows neutrinos to pass through the core. The left panel corresponds to the 1D modifications where the modification in density jump at CMB alters the  $\nu_\mu$  survival probability patterns differently for SJ and LJ scenarios compared to the standard scenario. It maybe observed that the neutrino oscillation patterns deviate significantly from the standard scenario in the energy range of 3 – 6 GeV, which corresponds to the NOLR/parametric resonance. The right panel corresponds to the 2D modifications where the deviation in oscillation patterns of SJLC and LJSC scenarios compared to standard profile are observed in the energy ranges corresponding to the NOLR/parametric resonance (3 – 6 GeV) as well as MSW resonance (6 – 10 GeV). A comparison between the left and right panels shows

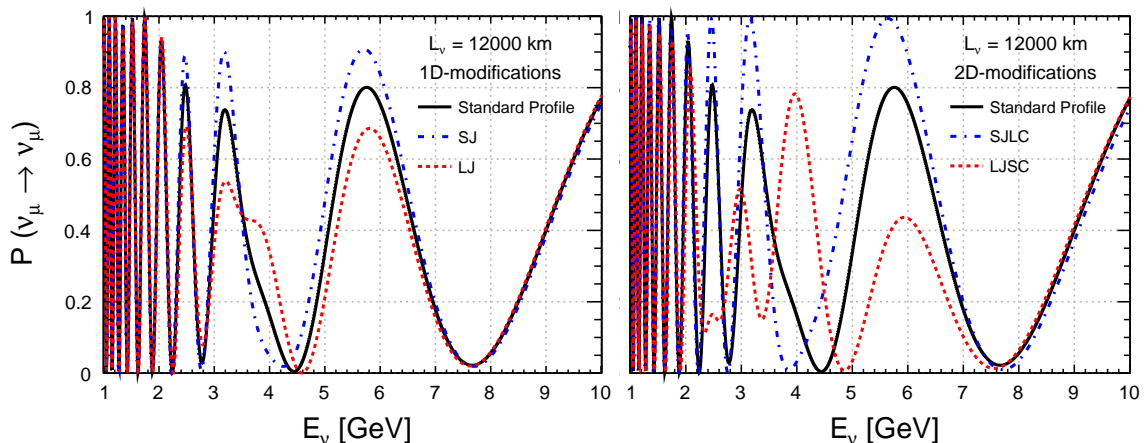


**Figure 2:** Three-flavor  $\nu_\mu \rightarrow \nu_\mu$  survival probabilities as functions of the neutrino energies ( $E_\nu$ ) for a baseline ( $L_\nu = 12000$  km) passing through the core. The solid black curves represent the scenario with the standard five-layered profile ( $\Delta\rho_{\text{CMB}} = 6.0$  g/cm<sup>3</sup> and  $R_{\text{CMB}} = 3480$  km). The left panel corresponds to the 1D modifications, where the dashed-blue and dotted-red curves represent the scenarios of SJ and LJ, respectively. The right panel corresponds to the 2D modifications, where the dashed-blue and dotted-red curves represent the scenarios of SJLC and LJSC, respectively. The modifications for SJ, LJ, SJLC, and LJSC scenarios are defined in Table 1. The values of neutrino oscillation parameters are taken from Table 2 assuming mass ordering to be NO.

that the neutrino oscillation patterns are sensitive to the different type of modifications in 1D and 2D and would be able to distinguish the modification of the density jump at CMB from that of the location of CMB.

### 2.3 Effect of modified density jumps and location of CMB on oscillograms

Neutrino oscillation patterns depend upon neutrino energies and baselines. Let us see the effects of modifications of the density jump at CMB and the location of CMB on  $\nu_\mu$  survival probability,  $P(\nu_\mu \rightarrow \nu_\mu)$ , in the  $(E_\nu, \cos\theta_\nu)$  plane. For the standard scenario of  $\Delta\rho_{\text{CMB}} = 6.0$  g/cm<sup>3</sup> and  $R_{\text{CMB}} = 3480$  km, we present the three-flavor  $\nu_\mu \rightarrow \nu_\mu$  survival probability oscillograms for neutrinos (left panel) and antineutrinos (right panel) assuming NO in Fig. 3. We consider the neutrino energy range of 1 – 25 GeV, and the cosine of zenith angle ( $\cos\theta_\nu$ ) from -1 to 0 for each panel. The black diagonal band which starts from  $(E_\nu = 1$  GeV,  $\cos\theta_\nu = 0$ ) and ends at  $(E_\nu = 25$  GeV,  $\cos\theta_\nu = -1$ ), represents the first oscillation minimum, which is also named as the “oscillation valley” [128, 129]. In the left panel, the region with significant matter effects can be observed in the form of a red patch around  $-0.8 < \cos\theta_\nu < -0.5$  and  $6$  GeV  $< E_\nu < 10$  GeV, which corresponds to the MSW resonance, whereas the yellow patches around  $\cos\theta_\nu < -0.8$  and  $3$  GeV  $< E_\nu < 6$  GeV are due to the NOLR/ parametric resonance. In the right panel, we do not see these matter effects for antineutrinos since the mass ordering is NO. However, this trend would be opposite for the inverted mass ordering where significant matter effects would be

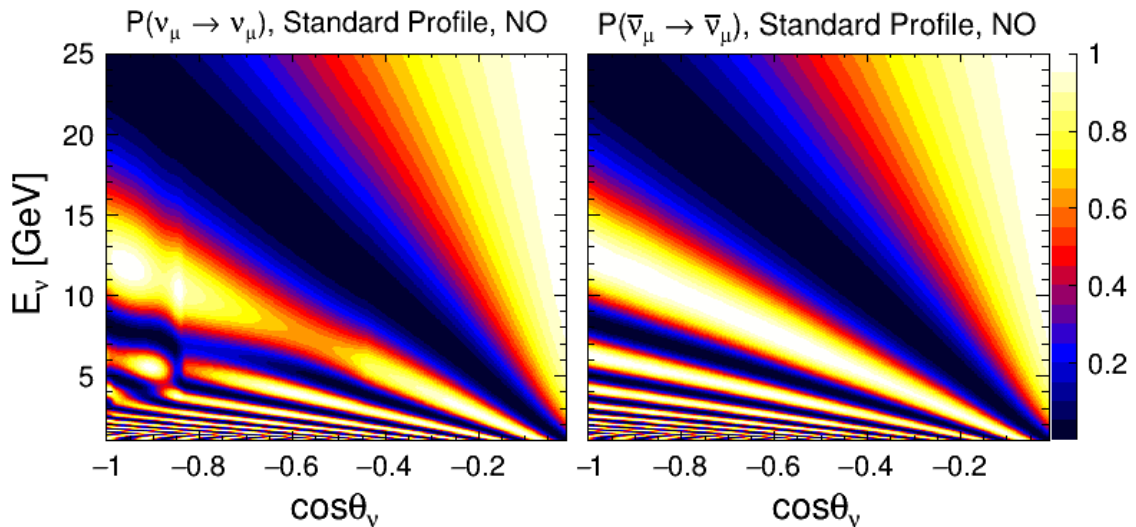


**Figure 3:** Three-flavor  $\nu_\mu \rightarrow \nu_\mu$  survival probability oscillograms for the standard five-layered profile with the standard density jump ( $\Delta\rho_{\text{CMB}} = 6.0 \text{ g/cm}^3$ ) and the standard CMB radius ( $R_{\text{CMB}} = 3480 \text{ km}$ ). The left and right panels correspond to neutrinos and antineutrinos, respectively. The values of neutrino oscillation parameters are taken from Table 2 assuming mass ordering to be NO.

observed for antineutrinos. In this section, we will focus on the neutrino survival channel with NO.

To start with, we demonstrate how the  $\nu_\mu$  survival probability oscillograms get affected due to the modifications in the density jump at CMB and the location of CMB in 1D and 2D. The top and bottom rows in Fig. 4 show the  $\nu_\mu$  survival probability oscillograms for the 1D and 2D modifications, respectively. The top left (right) panel corresponds to the SJ (LJ) scenarios, while the bottom left (right) panel corresponds to the SJLC (LJSC) scenarios, as described in Table 1. The observations are as follows:

- Comparing the oscillograms in the top row of Fig. 4 with the left panel of Fig. 3, we observe that for both SJ and LJ scenarios, the probability changes occur in the NOLR/parametric resonance region. For SJ (LJ) scenario, the MSW resonance region shrinks (stretches).
- The yellow patch in the NOLR/parametric resonance region becomes wider in the SJLC scenario in the bottom left panel of Fig. 4, compared to the standard case of the left panel of Fig. 3. On the other hand, the MSW resonance region is observed to shrink in the SJLC scenario.
- In the LJSC scenario depicted in the bottom right panel of Fig. 4, there are three yellow patches in the NOLR/parametric resonance region, while in the standard case (the left panel of Fig. 3), there is only one big yellow patch. The MSW resonance region is also observed to stretch in the LJSC scenario.

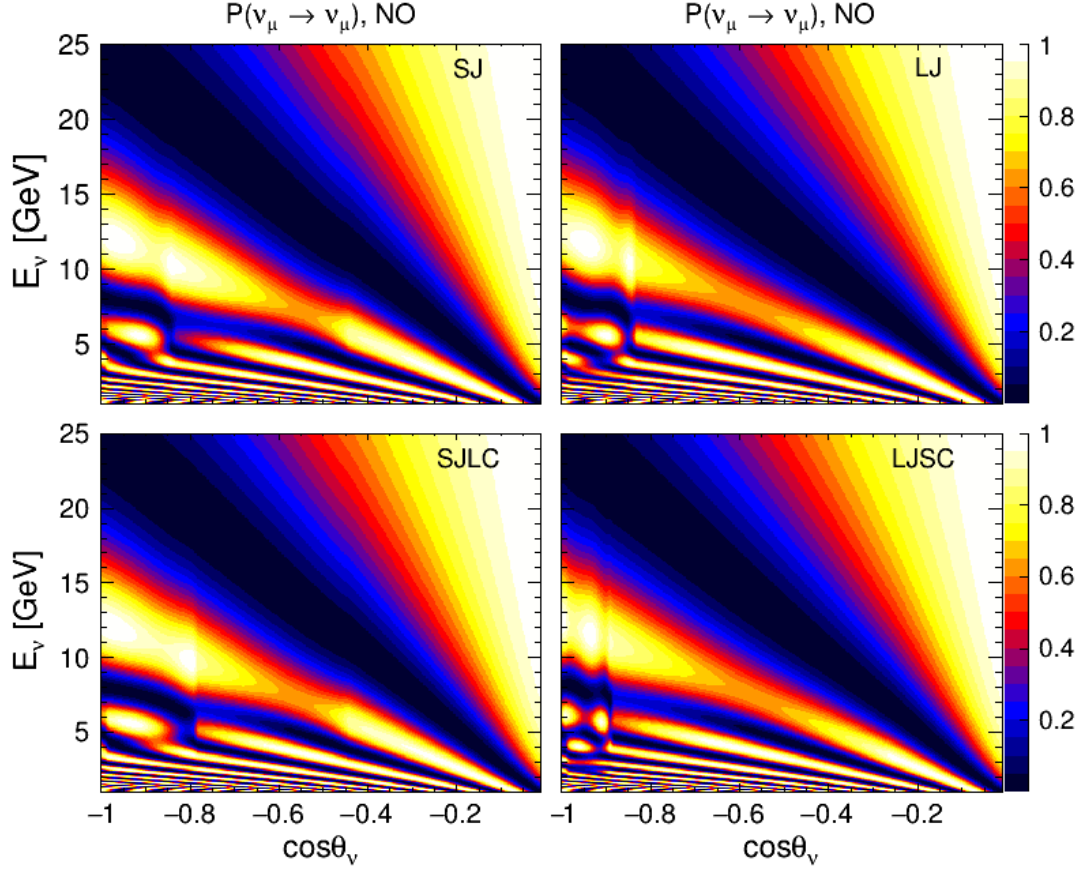


**Figure 4:** Three-flavor  $\nu_\mu \rightarrow \nu_\mu$  survival probability oscillograms with modified density jump and  $R_{\text{CMB}}$ . The top panels correspond to the 1D modifications, where the top-left (top-right) panel represents the scenario of SJ (LJ). The bottom panels correspond to the 2D modifications, where the bottom-left (bottom-right) panel represents the SJLC (LJSC) scenario. The modifications for SJ, LJ, SJLC, and LJSC scenarios are defined in Table 1. The values of neutrino oscillation parameters are taken from Table 2 assuming mass ordering to be NO.

For a better understanding, we present the probability differences between the 1D (2D) modifications and the standard scenario in the top (bottom) panels of Fig. 5. The top left (right) panel shows the distribution of  $\Delta P_{\text{SJ}}$  ( $\Delta P_{\text{LJ}}$ ), and the bottom left (right) panel shows the distribution of  $\Delta P_{\text{SJLC}}$  ( $\Delta P_{\text{LJSC}}$ ), which are defined as

$$\Delta P_{\text{SJ}} = P(\nu_\mu \rightarrow \nu_\mu)_{\text{SJ}} - P(\nu_\mu \rightarrow \nu_\mu)_{\text{standard}}, \quad (2.6)$$

$$\Delta P_{\text{LJ}} = P(\nu_\mu \rightarrow \nu_\mu)_{\text{LJ}} - P(\nu_\mu \rightarrow \nu_\mu)_{\text{standard}}, \quad (2.7)$$

$$\Delta P_{\text{SJLC}} = P(\nu_\mu \rightarrow \nu_\mu)_{\text{SJLC}} - P(\nu_\mu \rightarrow \nu_\mu)_{\text{standard}}, \quad (2.8)$$

$$\Delta P_{\text{LJSC}} = P(\nu_\mu \rightarrow \nu_\mu)_{\text{LJSC}} - P(\nu_\mu \rightarrow \nu_\mu)_{\text{standard}}. \quad (2.9)$$

The top panels of Fig. 5 show that the probability differences in the 1D scenarios SJ and LJ are significant for the core-passing neutrinos as well as for a fraction of the neutrinos that pass only through the mantle. This can be explained by the fact that the densities

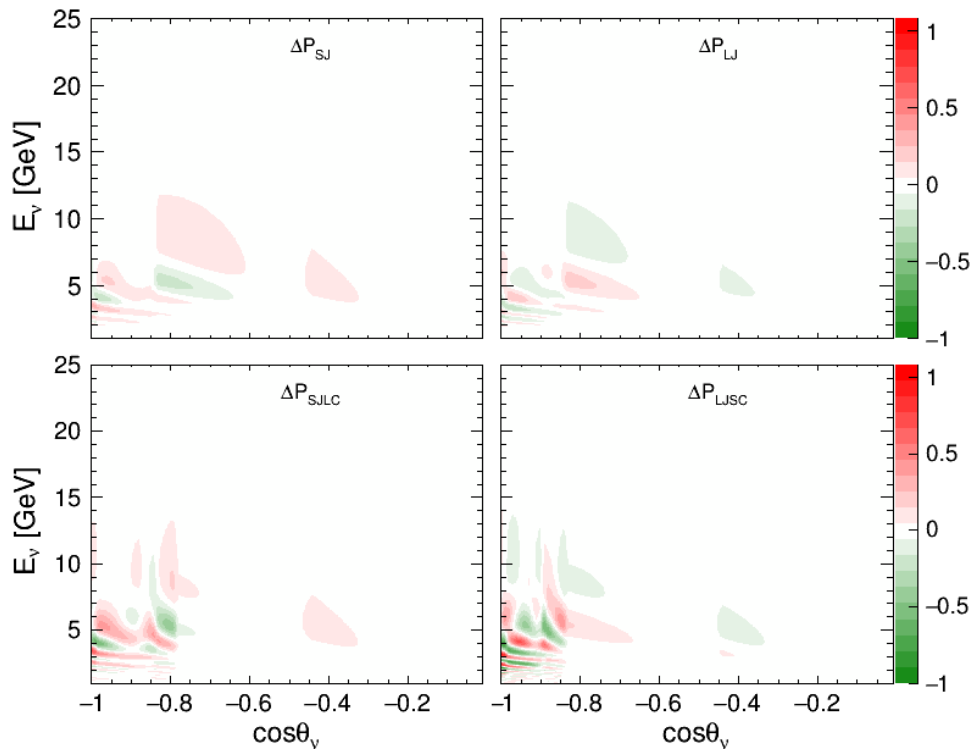


**Figure 5:** Oscillograms for the three-flavor  $\nu_\mu$  survival probability difference  $\Delta P(\nu_\mu \rightarrow \nu_\mu)$  for 1D (top panels) and 2D (bottom panels) modifications assuming the five-layered profile. The top left (right) panel corresponds to  $\Delta P(\nu_\mu \rightarrow \nu_\mu)$  between the SJ (LJ) scenario and the standard profile as defined in Eq. 2.6 (Eq. 2.7). The bottom left (right) panel corresponds to  $\Delta P(\nu_\mu \rightarrow \nu_\mu)$  between the SJLC (LJSC) scenario and the standard profile as defined in Eq. 2.8 (Eq. 2.9). The modifications for SJ, LJ, SJLC, and LJSC scenarios are defined in Table 1. The values of neutrino oscillation parameters are taken from Table 2 assuming mass ordering to be NO.

of both the core and the mantle are altered in the 1D-modifications (see Table 1). On the other hand, the bottom panels of Fig. 5 for the 2D-modifications SJLC and LJSC show that the probability differences are significant mainly for the neutrinos that pass through the core or very close to the core.

From Figs. 3, 4, and 5, we infer that the effects of modifications in the density jump at CMB and the location of CMB occur mainly at lower energies and larger baselines, since these long baselines would correspond to atmospheric neutrinos having trajectories with  $\cos\theta_\nu \lesssim -0.8$ . A detector like ICAL, with the help of its excellent angular resolution in the multi-GeV range of energy, would be able to probe the density jump and CMB radius simultaneously.

### 3 Atmospheric neutrinos at INO-ICAL

The proposed 50 kton iron calorimeter (ICAL) detector at the India-based Neutrino Observatory (INO) [123] is designed to detect multi-GeV atmospheric neutrinos and antineutrinos

separately over a wide range of baselines. ICAL would have three modules of size  $16\text{ m} \times 16\text{ m} \times 14.5\text{ m}$ , each having about 151 layers of iron plates of thickness 5.4 cm. The iron layers would be vertically stacked with a gap of about 4 cm where the glass Resistive Plate Chambers (RPCs) of size  $2\text{ m} \times 2\text{ m}$  would be inserted. The iron layers would act as a passive detector element providing a target material for the neutrino interactions, whereas RPCs would act as active detector element which would detect secondary charged particles produced in the neutrino interactions.

The charged-current interactions of muon neutrinos ( $\nu_\mu$ ) and antineutrinos ( $\bar{\nu}_\mu$ ) produce  $\mu^-$  and  $\mu^+$ , respectively. The muons are minimum ionizing particles in the multi-GeV energy range, and hence, they deposit energy in the detector the form of a long track. The magnetic field of about 1.5 T [130] would enable ICAL to distinguish  $\mu^-$  and  $\mu^+$  by observing the direction of curvature of muon track, and hence, to identify the parent  $\nu_\mu$  or  $\bar{\nu}_\mu$ . This charge identification capability (CID) of ICAL would play an essential role in the analyses driven by matter effects, such as the determination of the neutrino mass ordering, the measurement of the octant of  $\theta_{23}$ , and neutrino oscillation tomography. The time resolution of RPCs at ns level [131–133] would help ICAL to distinguish the upward-going and downward-going events. In the energy range of 1 - 25 GeV, ICAL would be able to measure the direction of muon ( $\cos\theta_\mu$ ) with an excellent angular resolution of about  $1^\circ$  [134] and the energy of muon ( $E_\mu$ ) with a resolution of about 10 – 15% [134].

In the multi-GeV range of energies, neutrinos can also undergo deep-inelastic scattering (DIS) which produce hadrons along with leptons. The hadrons deposit energy in the detector in the form of a shower. The hadrons can carry a significant fraction of incoming neutrino energy ( $E_\nu$ ). The hadron energy deposited in the detector can be defined as  $E'_{\text{had}} = E_\nu - E_\mu$ . ICAL would be able to measure the hadron energy with a resolution of about 40% for  $E'_{\text{had}} > 5\text{ GeV}$  [135].

In the present work, the unoscillated atmospheric neutrino events at ICAL are simulated using NUANCE [136] Monte Carlo (MC) neutrino event generator which takes the input in the form of ICAL geometry, and the Honda 3D flux of atmospheric neutrinos at the proposed INO site at Theni [137, 138]. The effect of solar modulation on the atmospheric neutrino flux has been taken into account by using neutrino flux with the high solar activity for half the exposure and with the low solar activity for the other half. A rock overburden of at least 1 km (3800 m water equivalent) from all directions at the INO site would reduce the cosmic muon background by a factor of about  $10^6$  [139]. Additionally, to veto muon tracks entering from outside the detector, the analyses at ICAL consider only those events for which the event vertices are completely inside the detector and far from the edges. Therefore, at ICAL, we expect negligible background due to downward-going cosmic muons. The interactions of tau neutrinos produce tau leptons which can decay into muons. The number of these muon events is only about 2% of the total upward-going muons from  $\nu_\mu$  interactions and most of them have lower energies which is below the energy threshold ( $\sim 1\text{ GeV}$ ) of ICAL. Therefore, we do not consider these muon events from tau decay in the present analysis. Since we evaluate median sensitivities in this analysis, we generate the unoscillated MC neutrino events for a large exposure of about 1000 years to suppress the statistical fluctuations. We incorporate the three-flavor neutrino oscillations

	1D modifications		2D modifications		Standard Case
	SJ	LJ	SJLC	LJSC	
$\mu^-$ events	8860	8840	8876	8841	8848
$\mu^+$ events	4031	4036	4032	4034	4033

**Table 3:** The total expected number of reconstructed  $\mu^-$  and  $\mu^+$  events using 1 Mt-yr exposure of the ICAL detector for the 1D modifications, 2D modifications, and standard case.

in the presence of Earth’s matter effects using the reweighting algorithm [140–142].

The detector responses for muons [134] and hadrons [135] have been incorporated using the migration matrices provided by the ICAL collaboration. The reconstruction efficiency, charge identification (CID) efficiency, energy resolution, and angular resolution of the ICAL detector for reconstructed muons are mentioned in figures 13, 14, 11, and 6, respectively, of Ref. [134]. After incorporating the detector responses, we obtain reconstructed observables such as the muon energy ( $E_\mu^{\text{rec}}$ ), the muon direction ( $\cos\theta_\mu^{\text{rec}}$ ), and the hadron energy ( $E_{\text{had}}^{\text{rec}}$ ) [140].

For the evaluation of sensitivities, the reconstructed events are scaled down from 1000-yr MC to 20-yr MC which corresponds to 1 Mt-yr exposure of ICAL. In 20 years, ICAL is expected to observe about 8848 (4033) reconstructed  $\mu^-$  ( $\mu^+$ ) events considering the three-flavor neutrino oscillations with Earth’s matter effects, assuming the standard five-layered profile of Earth for the case of normal mass ordering. In Table 3, we show the expected number of reconstructed  $\mu^-$  and  $\mu^+$  events for 1 Mt-yr exposure of the ICAL detector for all four scenarios of 1D and 2D modifications, viz. SJ, LJ, SJLC, and LJSC, for normal mass ordering. It may be observed that the total number of events for these four scenarios are not significantly different. However, the good directional and energy resolution of the ICAL detector permits us to bin the expected events in terms of reconstructed observables  $E_\mu^{\text{rec}}$ ,  $\cos\theta_\mu^{\text{rec}}$ , and  $E_{\text{had}}^{\text{rec}}$ . The binned events distributions for these scenarios are expected to be significantly different and would give rise to the sensitivity of ICAL to distinguish among them.

Now, we explore the impact of density jump variations at the standard  $R_{\text{CMB}}$  (1D modifications) and the modified  $R_{\text{CMB}}$  (2D modifications) on the bin-wise distribution of reconstructed muon events at the ICAL detector. In order to demonstrate the distributions of event differences in Fig. 6, we use a binning scheme with 10 bins in  $E_{\mu^-}^{\text{rec}}$  consisting of 5 bins of 1 GeV in (1 – 5) GeV, 1 bin of 2 GeV in (5 – 7) GeV, 1 bin of 3 GeV in (7 – 10) GeV, and 3 bins of 5 GeV in (10 – 25) GeV, and 20 uniform bins for  $\cos\theta_{\mu^-}^{\text{rec}}$  in the range of -1 to 1. The events have been integrated over the observable  $E_{\text{had}}^{\text{rec}}$  in the range of 0 to 25 GeV. Since for normal mass ordering, Earth’s matter effects are significant for neutrinos, we choose to present the distributions of event differences only for reconstructed  $\mu^-$  events.

The top (bottom) panels of Fig. 6 show the distribution of event differences between the modified density jumps for 1D (2D) modifications and the standard density jump, in the plane of  $(E_{\mu^-}^{\text{rec}}, \cos\theta_{\mu^-}^{\text{rec}})$  for 1 Mt-yr of exposure. The top left (right) panel present the distribution of event differences between the SJ (LJ) scenario and the standard density

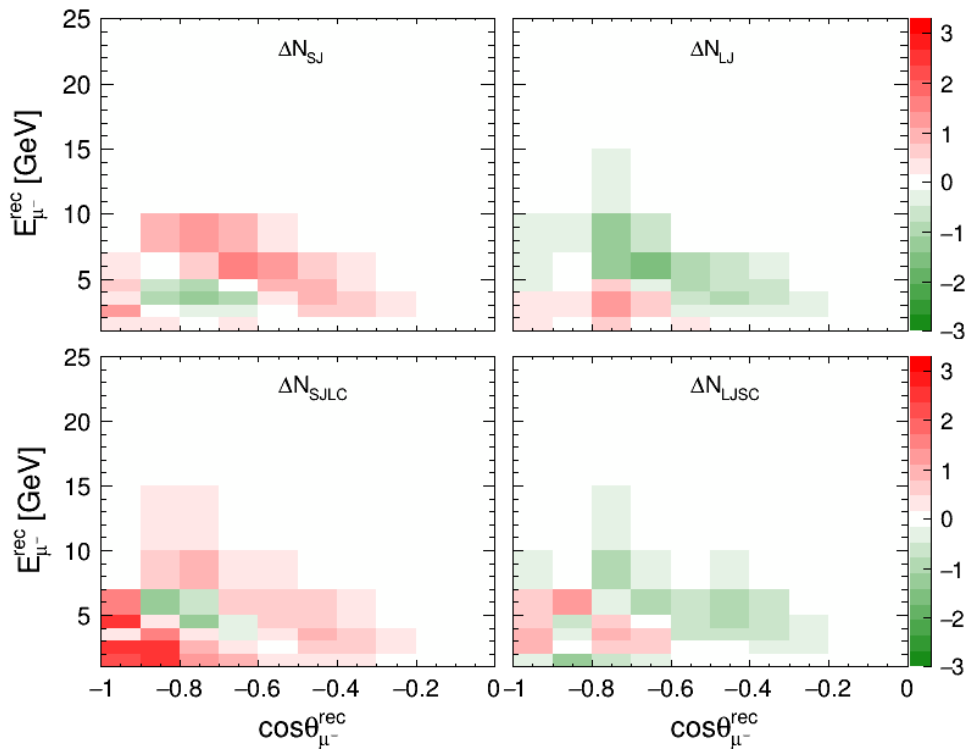


**Figure 6:** Distributions of reconstructed  $\mu^-$  event differences between the modified density jumps and the standard density jump in the plane of  $(E_{\mu^-}^{\text{rec}}, \cos \theta_{\mu^-}^{\text{rec}})$  for 1 Mt-yr exposure at ICAL. In top left (right) panel  $\Delta N_{\text{SJ}}$  ( $\Delta N_{\text{LJ}}$ ) represent the  $\mu^-$  event differences between the SJ (LJ) scenario and the standard density jump. In bottom left (right) panel,  $\Delta N_{\text{SJLC}}$  ( $\Delta N_{\text{LJSC}}$ ) denotes the  $\mu^-$  event differences between the SJLC (LJSC) scenario and the standard density jump. The modifications for SJ, LJ, SJLC, and LJSC scenarios are defined in Table 1. The values of neutrino oscillation parameters are taken from Table 2 assuming the mass ordering to be NO.

jump, while the bottom left (right) panel shows the distribution of event differences between the SJLC (LJSC) scenario and the standard density jump.

For 1D modifications, the event differences are observed to be significant in the core-passing neutrinos as well as the low-energy neutrinos that cross only the mantle, whereas the event differences are more prominent only for the core-passing neutrinos for 2D modifications. The smearing of these differences over a wider region in Fig. 6 as compared to Fig. 5 is mostly the result of the angular smearing caused by the deviation of the direction of reconstructed muon with respect to the true direction of the incoming neutrino during the interaction and event reconstruction.

## 4 Numerical analysis

In order to estimate the expected median sensitivity of ICAL for the correlated constraints on the density jumps and the location of CMB, we perform a  $\chi^2$  analysis in the frequentist approach [143]. We use a binning scheme optimized for matter effects in the Earth's

core [106]. The Poissonian  $\chi_-^2$  [144] for  $\mu^-$  is defined in term of reconstructed observables  $E_\mu^{\text{rec}}$ ,  $\cos\theta_\mu^{\text{rec}}$ , and  $E_{\text{had}}^{\text{rec}}$  as considered in Ref [140]:

$$\chi_-^2 = \min_{\xi_l} \sum_{i=1}^{N_{E_{\text{had}}^{\text{rec}}}} \sum_{j=1}^{N_{E_\mu^{\text{rec}}}} \sum_{k=1}^{N_{\cos\theta_\mu^{\text{rec}}}} \left[ 2(N_{ijk}^{\text{theory}} - N_{ijk}^{\text{data}}) - 2N_{ijk}^{\text{data}} \ln \left( \frac{N_{ijk}^{\text{theory}}}{N_{ijk}^{\text{data}}} \right) \right] + \sum_{l=1}^5 \xi_l^2, \quad (4.1)$$

with

$$N_{ijk}^{\text{theory}} = N_{ijk}^0 \left( 1 + \sum_{l=1}^5 \pi_{ijk}^l \xi_l \right). \quad (4.2)$$

Here  $N_{ijk}^{\text{theory}}$  and  $N_{ijk}^{\text{data}}$  denote the number of expected and observed reconstructed  $\mu^-$  events in a particular  $(E_\mu^{\text{rec}}, \cos\theta_\mu^{\text{rec}}, E_{\text{had}}^{\text{rec}})$  bin, respectively. The numbers  $N_{E_\mu^{\text{rec}}}$ ,  $N_{\cos\theta_\mu^{\text{rec}}}$ , and  $N_{E_{\text{had}}^{\text{rec}}}$  denote the total number of bins for each observables  $E_\mu^{\text{rec}}$ ,  $\cos\theta_\mu^{\text{rec}}$ , and  $E_{\text{had}}^{\text{rec}}$ , respectively. The variable  $N_{ijk}^0$  represents the number of expected events in a given bin without considering systematic uncertainties. In this work, we incorporate the following five systematic uncertainties [141, 142] using the well-known method of pulls [145–147]: (i) 20% flux normalization uncertainty, (ii) 5% energy dependent tilt error in flux, (iii) 5% zenith angle dependent tilt error in flux (iv) 10% uncertainty on cross section, and (v) 5% overall systematics. The pull variables for systematic uncertainties are given by  $\xi_l$  in Eqs. 4.1 and 4.2.

The  $\chi_+^2$  for reconstructed  $\mu^+$  events is also estimated following the same procedure as mentioned above. To estimate the resultant median sensitivity of the ICAL detector, we add the individual contributions of both  $\chi_-^2$  and  $\chi_+^2$  to get the total  $\chi^2$ :

$$\chi^2 = \chi_-^2 + \chi_+^2. \quad (4.3)$$

The MC data for this analysis is simulated using benchmark values of oscillation parameters given in Table 2 as true parameters. In the fit, we minimize  $\chi^2$  over the pull variables  $\xi_l$ . Since we estimate the sensitivity for 20 years of ICAL data and by that time, the oscillation parameters will be measured with high precision, we keep the oscillation parameters fixed at their benchmark values given in Table 2.

## 5 Results

In this section, we present the sensitivity of the proposed ICAL detector for the density jumps and the location of CMB. We simulate the MC data assuming the five-layered density profile of Earth with the standard density jumps and the standard radii of IC, OC, IM, MM, and Earth.

### 5.1 Constraining correlated density jumps assuming the standard CMB location

We quantify the expected sensitivity of the ICAL detector for measuring the density jumps keeping the standard location of CMB fixed (1D modifications) as follows:

$$\Delta\chi_{\text{1D-DJ}}^2 = \chi^2(\text{modified } \Delta\rho) - \chi^2(\text{standard } \Delta\rho), \quad (5.1)$$

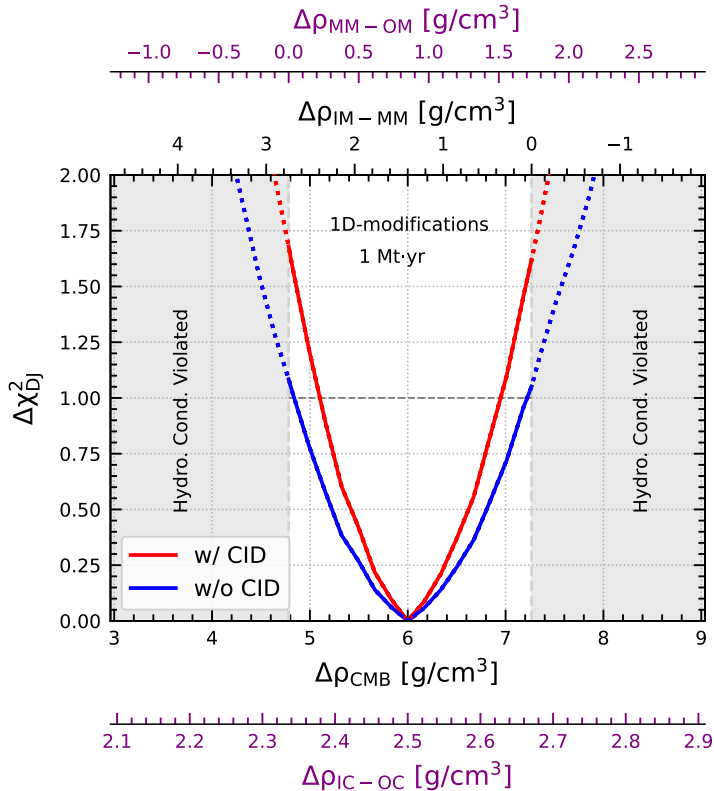


**Figure 7:** The median  $\Delta\chi_{\text{DJ}}^2$  as functions of the density jumps at the corresponding boundaries assuming the standard CMB location (1D modifications) for 1 Mt·yr exposure at ICAL. The top (bottom) two x-axes present the density jumps at the MM-OM and IM-MM (CMB and IC-OC) boundaries. The gray area represent the unphysical region where the hydrostatic equilibrium condition is violated. The red (blue) curve represents the sensitivity with (without) the CID capability of ICAL.  $\Delta\chi_{\text{DJ}}^2$  is minimized over systematic uncertainties, however, the oscillation parameters are kept fixed at their benchmark values given in Table 2 assuming the mass ordering to be NO.

where, DJ stands for “density jump” which is denoted by  $\Delta\rho$ . The sensitivity evaluated using  $\Delta\chi_{\text{DJ}}^2$  corresponds to a correlated measurement of four density jumps at the IC-OC, OC-IM (CMB), IM-MM, and MM-OM boundaries. Clearly,  $\Delta\rho$  can be interpreted in terms of  $\Delta\rho_{\text{IC-OC}}$ ,  $\Delta\rho_{\text{CMB}}$ ,  $\Delta\rho_{\text{IM-MM}}$ , or  $\Delta\rho_{\text{MM-OM}}$ .

Figure 7 shows the expected sensitivity of the ICAL detector in terms of  $\Delta\chi_{\text{DJ}}^2$  as functions of density jumps at the corresponding boundaries with an exposure of 1 Mt·yr. The red (blue) curve corresponds to the expected sensitivity with (without) the CID capability of the ICAL detector. We present the sensitivity in terms of the four x-axes corresponding to the above-mentioned four density jumps. The top two x-axes present the density jumps at the MM-OM and IM-MM boundaries, while the bottom two x-axes correspond to that at the CMB and IC-OC boundary. The gray areas represent the unphysical regions where the hydrostatic equilibrium condition is violated. We can observe that some parts of the red and blue curves lie in the gray region, which are denoted by the dotted curves. From

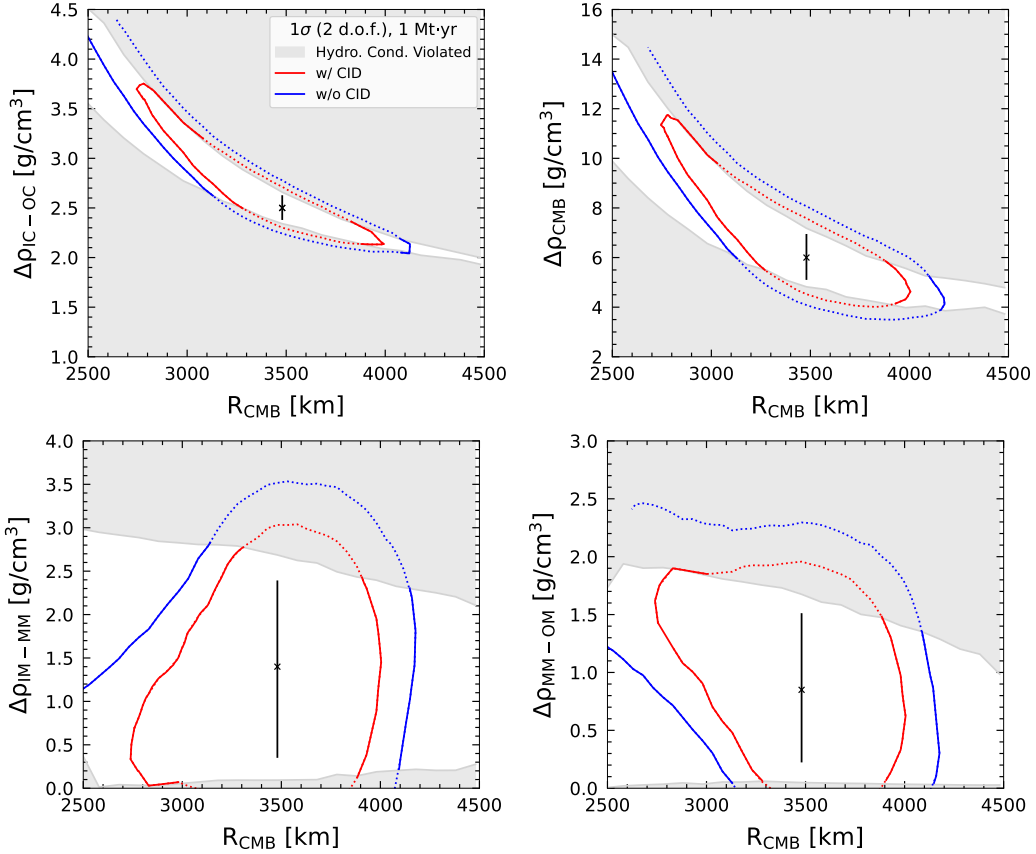


**Figure 8:** The median  $\Delta\chi_{\text{DJ-CMB}}^2$  sensitivity contours in the plane of the density jumps and the location of CMB radius at  $1\sigma$  (2 d.o.f.) for 1 Mt-yr exposure. The red (blue) contour corresponds to the sensitivity with (without) the CID capability of the ICAL detector. The gray areas represent the unphysical region where the hydrostatic equilibrium condition is violated. The black crosses and vertical bars represent the standard values and  $1\sigma$  constraints for the density jumps, respectively, assuming standard  $R_{\text{CMB}} = 3480$  km for 1D modifications as shown in Fig. 7.  $\Delta\chi_{\text{DJ-CMB}}^2$  is minimized over systematic uncertainties; however, the oscillation parameters are kept fixed at their benchmark values given in Table 2 assuming the mass ordering to be NO.

the red curve in Fig. 7, we can observe that the ICAL detector would be able to constrain the value of the density jump at the CMB ( $\Delta\rho_{\text{CMB}}$ ) to be  $[5.1, 7.0]$  g/cm<sup>3</sup> at  $1\sigma$ . This corresponds to a precision of about 15%. The CID capability of the ICAL detector would play an important role in this precision. In the absence of CID (blue curve), the sensitivity range would deteriorate to  $[4.8, 7.2]$  g/cm<sup>3</sup> at  $1\sigma$ , which corresponds to a precision of about 20%. We have checked that these sensitivities for the density jumps remain almost the same even if we minimize over the relevant oscillation parameters in their allowed ranges in the fit.

## 5.2 Constraining correlated density jumps and location of CMB

In this section, we present the expected sensitivities for 2D modifications, where the correlated density jumps and the location of CMB radius are modified simultaneously. The ICAL sensitivity is quantified as

$$\Delta\chi_{\text{DJ-CMB}}^2 = \chi^2(\text{modified } \{\Delta\rho, R_{\text{CMB}}\}) - \chi^2(\text{standard } \{\Delta\rho, R_{\text{CMB}}\}). \quad (5.2)$$

The expected sensitivity of the ICAL detector for constraining the correlated density jumps and the location of CMB radius simultaneously is shown in Fig. 8 in terms of contours at  $1\sigma$  (2 d.o.f.) for the exposure of 1 Mt·yr. In this analysis,  $\Delta\chi_{\text{DJ-CMB}}^2$  is minimized over systematic uncertainties; however, the oscillation parameters are kept fixed at the benchmark values given in Table 2 and the mass ordering is taken to be NO. The top left (right) panel shows the sensitivity contour for simultaneously constraining the density jump at the IC-OC (CMB) boundary and the location of CMB radius, whereas the bottom left (right) panel presents the sensitivity for the density jump at the IM-MM (MM-OM) boundary and the location of CMB radius. The red (blue) contour shows the expected sensitivity with (without) the CID capability of the ICAL detector.

The light-gray region in each plot in Fig. 8 corresponds to the parameter space where the hydrostatic equilibrium condition is violated. For each plot, it is observed that some parts of the red and blue contours are present in the gray region, which are denoted by the dotted curves. The black cross symbols represent the standard values of the corresponding density jumps and the location of CMB radius. The black vertical bars denote the  $1\sigma$  bounds on the density jumps at the standard CMB radius for 1D modifications, which are obtained from Fig. 7.

Note that, in the context of the five-layered model of Earth, the white region in Fig. 8 is allowed by the measurements of  $M_E$ ,  $I_E$ , the density  $\rho_{\text{OM}}$ , the radii  $R_{\text{IC}}$ ,  $R_{\text{IM}}$ ,  $R_{\text{MM}}$ ,  $R_E$ , and the density ratio  $\rho_{\text{IC}}/\rho_{\text{OC}}$ . In this work, we demonstrate that the neutrino oscillation data can help us to further constrain the white region, which clearly shows the complementarity of our proposed method with the existing measurements of the above quantities.

## 5.3 Impact of different true choices of $\sin^2\theta_{23}$

So far, we have considered  $\sin^2\theta_{23}(\text{true}) = 0.5$  in our analysis. However, the present global fit indicates that  $\theta_{23}$  may not correspond to maximal mixing ( $\sin^2\theta_{23} = 0.5$ ). It can either lie in the lower octant ( $\sin^2\theta_{23} < 0.5$ ) or the higher octant ( $\sin^2\theta_{23} > 0.5$ ). Therefore, in this section, we discuss how the ICAL sensitivity for constraining the density jump and CMB radius may change if  $\theta_{23}(\text{true})$  is non-maximal.

To analyze the impact of the true value of  $\sin^2\theta_{23}$ , we demonstrate the expected sensitivity of the ICAL detector for measuring the density jumps with the standard CMB location (1D modifications) in Fig. 9. The violet, red, and green curves correspond to the sensitivities where MC data is generated using  $\sin^2\theta_{23}(\text{true}) = 0.4, 0.5, \text{ and } 0.6$ , respectively. In the fit,  $\sin^2\theta_{23}$  is kept fixed at its corresponding true value, whereas all other oscillation parameters are kept fixed at their benchmark values given in Table 2 assuming the mass ordering to be NO. The other details in Fig. 9 are same as in Fig. 7.

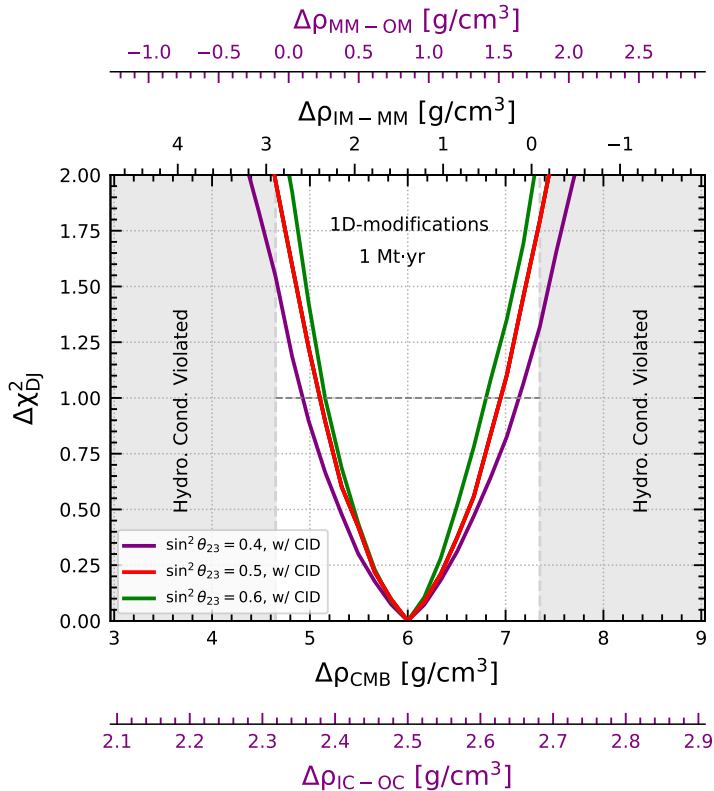


**Figure 9:** The median  $\Delta\chi_{\text{DJ}}^2$  as functions of the density jumps at the corresponding boundaries assuming the standard CMB location (1D modifications) for three choices of the true values of  $\sin^2 \theta_{23}$  with 1 Mt·yr exposure at ICAL. The top (bottom) two x-axes present the density jumps at the MM-OM and IM-MM (CMB and IC-OC) boundaries. The gray areas represent the unphysical regions where the hydrostatic equilibrium condition is violated. The violet, red, and green curves correspond to the sensitivities where MC data is generated using  $\sin^2 \theta_{23}(\text{true}) = 0.4, 0.5,$  and  $0.6$ , respectively.  $\Delta\chi_{\text{DJ}}^2$  is minimized over systematic uncertainties; however,  $\sin^2 \theta_{23}$  is kept fixed at its corresponding true value and all other oscillation parameters are kept fixed at their benchmark values given in Table 2 assuming the mass ordering to be NO.

We observe that the expected sensitivities of ICAL enhance (deteriorate) if the true value of  $\sin^2 \theta_{23} = 0.6$  ( $0.4$ ) compared to the maximal mixing case where  $\sin^2 \theta_{23} = 0.5$ .

In Figure 10, we present the effect of the true values of  $\sin^2 \theta_{23}$  on the expected sensitivities of the ICAL detector for constraining the correlated density jumps and the CMB location simultaneously (2D modifications). The violet, red, and green curves denote the sensitivities for  $\sin^2 \theta_{23}(\text{true}) = 0.4, 0.5,$  and  $0.6$ , respectively. In the fit, we keep the oscillation parameters fixed at their true values. The other details in Fig. 10 are same as in Fig. 8. We observe that the ICAL sensitivities enhance (deteriorate) if  $\theta_{23}(\text{true})$  belongs to higher (lower) octant.

From both the Figures 9 and 10, we observe that the expected ICAL sensitivities are larger (smaller) for higher (lower) octant. This happens because for NO, the dominant matter effect terms in  $P(\nu_\mu \rightarrow \nu_\mu)$  survival and  $P(\nu_e \rightarrow \nu_\mu)$  appearance probabilities are

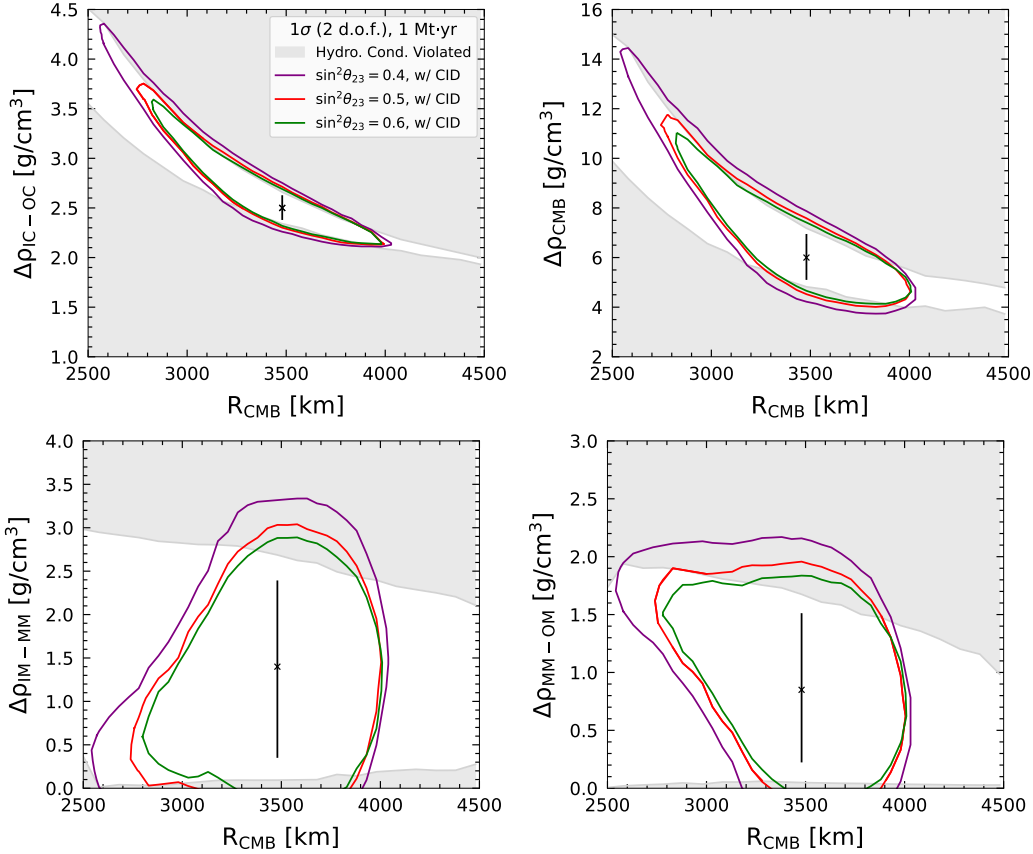


**Figure 10:** The median  $\Delta\chi_{\text{DJ-CMB}}^2$  sensitivity contours in the plane of the density jumps and the location of CMB radius at  $1\sigma$  (2 d.o.f.) for three choices of the true values of  $\sin^2\theta_{23}$  with 1 Mt-yr exposure. The violet, red, and green curves correspond to the sensitivities where MC data is generated using  $\sin^2\theta_{23}$  (true) = 0.4, 0.5, and 0.6, respectively. The gray areas represent the unphysical region where the hydrostatic equilibrium condition is violated. The black crosses and vertical bars represent the standard values and  $1\sigma$  constraints over density jumps, respectively, assuming standard  $R_{\text{CMB}} = 3480$  km for 1D modifications as shown in Fig. 7.  $\Delta\chi_{\text{DJ}}^2$  is minimized over systematic uncertainties; however,  $\sin^2\theta_{23}$  is kept fixed at its corresponding true value and all other oscillation parameters are kept fixed at their benchmark values given in Table 2 assuming the mass ordering to be NO.

proportional to  $\sin^2\theta_{23}$  as shown by the series expansion in Ref. [148]. With increase in  $\sin^2\theta_{23}$ , the survival probability  $P(\nu_\mu \rightarrow \nu_\mu)$  decreases, whereas the appearance probability  $P(\nu_e \rightarrow \nu_\mu)$  increases. Since the flux of  $\nu_\mu$  is larger than that of  $\nu_e$ , the decrease in the contribution of the survival ( $\nu_\mu \rightarrow \nu_\mu$ ) channel is more than the increase in that of the appearance ( $\nu_e \rightarrow \nu_\mu$ ) channel. Therefore, the resultant matter effect does not wash out completely and is proportional to  $\sin^2\theta_{23}$ . This indicates that the ICAL detector would be able to constrain the density jump and CMB location with higher confidence if  $\theta_{23}$  in nature is in the higher octant.

## 6 Summary and conclusions

The internal structure of Earth has been extensively studied through the traditional methods such as gravitational and seismological measurements. In this paper, we utilize a completely different method to explore the internal structure of Earth, which relies on weak interactions of neutrinos. This is broadly known as neutrino tomography of Earth. Using neutrinos as an independent and complementary tool would pave the way for the “multi-messenger tomography of Earth”, which would enhance our understanding of Earth’s internal structure.

Neutrino propagation through Earth is affected by the interactions of neutrinos with matter which depend on the energies of neutrinos. Neutrinos having energies of a few TeV undergo inelastic scattering with the ambient nucleons, leading to the absorption of neutrinos inside Earth, which can be used to probe the density distribution inside Earth. This method is known as neutrino absorption tomography.

The other way of probing the internal structure of Earth is via matter effects in neutrino flavor transition. The multi-GeV atmospheric neutrinos undergo elastic forward scattering with the ambient electrons while passing through Earth. These matter effects depend upon the energy and electron number density in the path of neutrinos, and alter the neutrino oscillation probabilities. Neutrinos with energies 6–10 GeV experience the MSW resonance while passing through the mantle, whereas neutrinos with energies 3–6 GeV that pass through the high-density core experience neutrino oscillation length resonance (NOLR) / parametric resonance (PR). These matter effects, particularly the NOLR/PR resonance, depend on the density jump at the core-mantle boundary (CMB) and its location, which in turn can alter neutrino oscillation probabilities.

An atmospheric neutrino detector can be sensitive to the value of the density jump at CMB ( $\Delta\rho_{\text{CMB}}$ ) and the CMB radius ( $R_{\text{CMB}}$ ) by detecting the modified neutrino oscillation patterns. In the present work, we study the effect of modifying  $\Delta\rho_{\text{CMB}}$  and  $R_{\text{CMB}}$  on the neutrino oscillation probabilities and expected neutrino event distributions. We estimate the sensitivity of the proposed ICAL detector to probe the correlated constraints on  $\Delta\rho_{\text{CMB}}$  and  $R_{\text{CMB}}$ .

In this work, we use a five-layered density model of Earth, which is a simplified form of the PREM profile. The five distinct layers are the inner core (IC), the outer core (OC), the inner mantle (IM), the middle mantle (MM), and the outer mantle (OM). In this five-layered model, the four significant density jumps occur at the following boundaries: the inner core - outer core (IO-OC) boundary, the outer core - inner mantle (OC-IM) boundary, also known as CMB, the inner mantle - middle mantle (IM-MM) boundary, and the middle mantle - outer mantle (MM-OM) boundary. We ensure that the mass and moment of inertia of Earth do not change while modifying the density jumps and the CMB location. As an additional constraint, we take the density of outer mantle to be completely known, and use a fixed value for the ratio of densities of the inner and outer cores. Apart from these constraints, the hydrostatic equilibrium condition is also imposed throughout the calculation. The five-layered profile with the above-mentioned constraints allows us to perform two kind of modifications: (i) 1D modifications of the density jump at CMB with

the fixed standard CMB location, and (ii) 2D modifications of the density jump at CMB as well as its location.

We study the effects of the 1D and 2D modifications on neutrino oscillation probabilities and event distributions at ICAL for some representative scenarios. In 1D modifications, we demonstrate two scenarios, namely, a smaller jump (SJ) and a larger Jump (LJ). For these scenarios, the effects of these modifications on the  $\nu_\mu \rightarrow \nu_\mu$  survival probability are found to be mainly in the NOLR/PR resonance region. In 2D modifications, we explore two scenarios, namely, a smaller jump at a larger core (SJLC) and a larger jump at a smaller core (LJSC). For these scenarios, the effects of these modifications on the  $\nu_\mu \rightarrow \nu_\mu$  survival probability are found in both the NOLR/PR and the MSW resonance regions. The ICAL detector, with its excellent energy and direction resolution, would be able to detect these features and probe the density jump and the CMB location simultaneously.

We quantify the expected sensitivity of the ICAL detector for determining the density jump at CMB and its location for both 1D and 2D modifications. Using the five-layered density profile, we simulate the prospective data with the standard density jump and CMB radius. The statistical significance to measure the density jump at the standard CMB location is calculated in terms of median  $\Delta\chi^2$  by fitting the prospective data with the modified density jump in theory. We observe that the ICAL detector would be able to measure the density jump at CMB with a precision of about 15% at  $1\sigma$  with 1 M-yr exposure. The CID capability of the ICAL detector would play a significant role in this precision; in the absence of CID,  $1\sigma$  sensitivity deteriorates to about 20%. Exploiting the 2D-modifications, we present the  $1\sigma$  sensitivity contours to simultaneously constrain the density jump at CMB and its location with and without CID capability of the ICAL detector. Since the densities of all the layers modify simultaneously during variation of density jump at CMB due to constraints, these results can also be interpreted in terms of the precisions on the density jumps at the other layer boundaries such as IC-OC, IM-MM, and MM-OM. These sensitivities show that the neutrino oscillation data can further constrain the parameter space allowed by the measurements of  $M_E$ ,  $I_E$ , the density  $\rho_{OM}$ , the radii  $R_{IC}$ ,  $R_{IM}$ ,  $R_{MM}$ ,  $R_E$ , and the density ratio  $\rho_{IC}/\rho_{OC}$ .

In future, the next-generation atmospheric neutrino detectors like Hyper-K, ORCA, DUNE, IceCube/DeepCore/Upgrade, and P-ONE with a large statistics of neutrino data will significantly enhance the precision related to the density profile of Earth using weak interactions of neutrinos. The combined studies of the internal structure of Earth with the neutrino data will provide information independent of and complementary to that from the gravitational and seismological measurements.

## Acknowledgements

This study is performed by the INO-ICAL collaboration to explore the possibility of utilizing Earth’s matter effects in oscillations of atmospheric neutrinos to constrain the core radius and density jumps inside Earth simultaneously. We would like to thank S. Goswami for her useful comments and constructive suggestions on our work. A.K.U. would like to thank the organizers of the “International Workshop on Multi-messenger Tomography of the Earth (MMTE 2023)” at APC-Université Paris Cité in Paris, France, during 4th to 7th

July 2023, for providing an opportunity to present the preliminary results from this work. We acknowledge the support of the Department of Atomic Energy (DAE), Govt. of India, under the Project Identification Numbers RTI4002 and RIO 4001. S.K.A. acknowledges the financial support from the Swarnajayanti Fellowship (sanction order no. DST/SJF/PSA-05/2019-20) provided by the Department of Science and Technology (DST), Govt. of India, and the Research Grant (sanction order no. SB/SJF/2020-21/21) provided by the Science and Engineering Research Board (SERB), Govt. of India, under the Swarnajayanti Fellowship project. A.K.U. acknowledges financial support from the DST, Govt. of India (sanction order no. DST/INSPIRE Fellowship/2019/IF190755). The numerical simulations are performed using the “SAMKHYA: High-Performance Computing Facility” at the Institute of Physics, Bhubaneswar, India.

## References

- [1] J. C. Ries, R. J. Eanes, C. K. Shum, and M. M. Watkins, *Progress in the determination of the gravitational coefficient of the earth*, *Geophysical Research Letters* **19** (1992), no. 6 529–531, [<https://agupubs.onlinelibrary.wiley.com/doi/pdf/10.1029/92GL00259>].
- [2] B. Luzum, N. Capitaine, A. Fienga, W. Folkner, T. Fukushima, J. Hilton, C. Hohenkerk, G. Krasinsky, G. Petit, E. Pitjeva, M. Soffel, and P. Wallace, *The IAU 2009 system of astronomical constants: the report of the IAU working group on numerical standards for fundamental astronomy*, *Celestial Mechanics and Dynamical Astronomy* **110** (July, 2011) 293–304.
- [3] G. Rosi, F. Sorrentino, L. Cacciapuoti, M. Prevedelli, and G. M. Tino, *Precision Measurement of the Newtonian Gravitational Constant Using Cold Atoms*, *Nature* **510** (2014) 518, [[arXiv:1412.7954](https://arxiv.org/abs/1412.7954)].
- [4] USAO, USNO, HMNAO and UKHO *The Astronomical Almanac* (US Navy, 2020), <https://aa.usno.navy.mil/>, <http://asa.hmnao.com/>.
- [5] J. G. Williams, *Contribution to the earth’s obliquity rate, precession, and nutation*, *Astronomical Journal* **108** (Aug., 1994) 711.
- [6] W. Chen, J. C. Li, J. Ray, W. B. Shen, and C. L. Huang, *Consistent estimates of the dynamic figure parameters of the earth*, *Journal of Geodesy* **89** (Oct., 2014) 179–188.
- [7] B. Gutenberg, *Ueber Erdbebenwellen. VII A. Beobachtungen an Registrierungen von Fernbeben in Göttingen und Folgerung über die Konstitution des Erdkörpers (mit Tafel)*, *Nachrichten von der Gesellschaft der Wissenschaften zu Göttingen, Mathematisch-Physikalische Klasse* **1914** (1914) 125–176.
- [8] E. C. Robertson, *The interior of the Earth, an elementary description*, 1966.
- [9] M. Moser and L. Völgyesi, *The inner structure of the earth*, *Periodica Polytechnica Chemical Engineering* **26(3-4)** (1982) 155–204.
- [10] D. E. Loper and T. Lay, *The core-mantle boundary region*, *Journal of Geophysical Research: Solid Earth* **100** (1995), no. B4 6397–6420.
- [11] D. Alfé, M. J. Gillan, and G. D. Price, *Temperature and composition of the earth’s core*, *Contemporary Physics* **48** (2007), no. 2 63–80.

- [12] F. D. Stacey and P. M. Davis, *Physics of the Earth*. Cambridge University Press, 4 ed., 2008.
- [13] W. F. McDonough, *The internal structure of the earth*, 2022. Talk given at the Multi-messenger Tomography of Earth (MMTE 2022) Workshop, Salt Lake City, Utah, USA, [https://indico.fnal.gov/event/53004/contributions/245228/attachments/158242/207568/MMTE\\_30July-McDonough.pdf](https://indico.fnal.gov/event/53004/contributions/245228/attachments/158242/207568/MMTE_30July-McDonough.pdf).
- [14] M. Thorne, *An overview of the core-mantle boundary region from seismological studies*, 2022. Talk given at the Multi-messenger Tomography of Earth (MMTE 2022) Workshop, Salt Lake City, Utah, USA, [https://indico.fnal.gov/event/53004/contributions/247698/attachments/158241/207567/2022\\_Thorne\\_MMTE\\_noT.pptx](https://indico.fnal.gov/event/53004/contributions/247698/attachments/158241/207567/2022_Thorne_MMTE_noT.pptx).
- [15] K. Hirose, *Chemical composition and hydrogen content inside earth*, 2022. Talk given at the Multi-messenger Tomography of Earth (MMTE 2022) Workshop, Salt Lake City, Utah, USA, [https://indico.fnal.gov/event/53004/contributions/245136/attachments/158243/207573/220730%20MMTE%20workshop\\_Hirose%20final.pdf](https://indico.fnal.gov/event/53004/contributions/245136/attachments/158243/207573/220730%20MMTE%20workshop_Hirose%20final.pdf).
- [16] W. F. McDonough, *Structure and composition of the earth*, 2023. Talk given at the International Workshop on Multi-messenger Tomography of the Earth (MMTE 2023), APC, Paris, France, [https://indico.in2p3.fr/event/30001/contributions/126042/attachments/78912/115264/MMTE\\_4July-McDonough.pptx](https://indico.in2p3.fr/event/30001/contributions/126042/attachments/78912/115264/MMTE_4July-McDonough.pptx).
- [17] W. McDonough, *Compositional Model for the Earth's Core*, in *Treatise on Geochemistry* (H. D. Holland and K. K. Turekian, eds.), pp. 559–577. Elsevier, Oxford, second ed., 2014.
- [18] I. Lehmann, *P', Bureau Central Séismologique International Strasbourg: Publications du Bureau Central Scientifiques* **14** (1936) 87–115.
- [19] A. F. Birch, *The alpha-gamma transformation of iron at high pressures, and the problem of the earth's magnetism*, *American Journal of Science* **238** (1940), no. 3 192–211.
- [20] F. Gilbert and A. M. Dziewonski, *An Application of Normal Mode Theory to the Retrieval of Structural Parameters and Source Mechanisms from Seismic Spectra*, *Philosophical Transactions of the Royal Society of London Series A* **278** (Mar., 1975) 187–269.
- [21] A. Dziewonski, A. Hales, and E. Lapwood, *Parametrically simple earth models consistent with geophysical data*, *Physics of the Earth and Planetary Interiors* **10** (1975), no. 1 12–48.
- [22] B. L. N. Kennett and E. R. Engdahl, *Traveltimes for Global Earthquake Location and Phase Identification*, *Geophysical Journal International* **105** (May, 1991) 429–465.
- [23] B. L. N. Kennett, E. R. Engdahl, and R. Buland, *Constraints on seismic velocities in the Earth from traveltimes*, *Geophysical Journal International* **122** (July, 1995) 108–124.
- [24] F. Cammarano, A. Deuss, S. Goes, and D. Giardini, *One-dimensional physical reference models for the upper mantle and transition zone: Combining seismic and mineral physics constraints*, *Journal of Geophysical Research: Solid Earth* **110** (2005), no. B1.
- [25] B. Kustowski, G. Ekström, and A. M. Dziewoński, *Anisotropic shear-wave velocity structure of the earth's mantle: A global model*, *Journal of Geophysical Research: Solid Earth* **113** (2008), no. B6.
- [26] A. M. Dziewonski and D. L. Anderson, *Preliminary reference earth model*, *Phys. Earth Planet. Interiors* **25** (1981) 297–356.
- [27] B. A. Bolt, *The precision of density estimation deep in the earth*, *Q. J. R. Astron. Soc.* **32** (12, 1991) 367.

- [28] B. L. N. Kennett, *On the density distribution within the Earth*, *Geophysical Journal International* **132** (02, 1998) 374–382.
- [29] G. Masters and D. Gubbins, *On the resolution of density within the earth*, *Physics of the Earth and Planetary Interiors* **140** (2003), no. 1 159–167.
- [30] Q. Williams and R. J. Hemley, *Hydrogen in the deep earth*, *Annual Review of Earth and Planetary Sciences* **29** (2001), no. 1 365–418, [<https://doi.org/10.1146/annurev.earth.29.1.365>].
- [31] K. Hirose, B. Wood, and L. Vočadlo, *Light elements in the earth’s core*, *Nature Reviews Earth & Environment* **2** (Sep, 2021) 645–658.
- [32] T. Araki et al., *Experimental investigation of geologically produced antineutrinos with KamLAND*, *Nature* **436** (2005) 499–503.
- [33] **Borexino** Collaboration, M. Agostini et al., *Spectroscopy of geoneutrinos from 2056 days of Borexino data*, *Phys. Rev. D* **92** (2015), no. 3 031101, [[arXiv:1506.04610](https://arxiv.org/abs/1506.04610)].
- [34] G. Bellini, K. Inoue, F. Mantovani, A. Serafini, V. Strati, and H. Watanabe, *Geoneutrinos and geoscience: an intriguing joint-venture*, *Riv. Nuovo Cim.* **45** (2022), no. 1 1–105, [[arXiv:2109.01482](https://arxiv.org/abs/2109.01482)].
- [35] **KamLAND** Collaboration, S. Abe et al., *Abundances of uranium and thorium elements in Earth estimated by geoneutrino spectroscopy*, *Geophysical Research Letters* **49** (5, 2022) e2022GL099566, [[arXiv:2205.14934](https://arxiv.org/abs/2205.14934)].
- [36] G. Fiorentini, M. Lissia, and F. Mantovani, *Geo-neutrinos and Earth’s interior*, *Phys. Rept.* **453** (2007) 117–172, [[arXiv:0707.3203](https://arxiv.org/abs/0707.3203)].
- [37] G. Bellini, A. Ianni, L. Ludhova, F. Mantovani, and W. F. McDonough, *Geo-neutrinos*, *Prog. Part. Nucl. Phys.* **73** (2013) 1–34, [[arXiv:1310.3732](https://arxiv.org/abs/1310.3732)].
- [38] S. T. Dye, Y. Huang, V. Lekic, W. F. McDonough, and O. Sramek, *Geo-neutrinos and Earth Models*, *Phys. Procedia* **61** (2015) 310–318, [[arXiv:1405.0192](https://arxiv.org/abs/1405.0192)].
- [39] M. Leyton, S. Dye, and J. Monroe, *Exploring the hidden interior of the earth with directional neutrino measurements*, *Nature Communications* **8** (July, 2017).
- [40] W. Winter, *Neutrino tomography: Learning about the earth’s interior using the propagation of neutrinos*, *Earth Moon Planets* **99** (2006) 285–307, [[physics/0602049](https://arxiv.org/abs/physics/0602049)].
- [41] M. C. Gonzalez-Garcia, F. Halzen, M. Maltoni, and H. K. M. Tanaka, *Radiography of earth’s core and mantle with atmospheric neutrinos*, *Phys. Rev. Lett.* **100** (2008) 061802, [[arXiv:0711.0745](https://arxiv.org/abs/0711.0745)].
- [42] A. Donini, S. Palomares-Ruiz, and J. Salvado, *Neutrino tomography of Earth*, *Nature Phys.* **15** (2019), no. 1 37–40, [[arXiv:1803.05901](https://arxiv.org/abs/1803.05901)].
- [43] W. Winter, *Atmospheric Neutrino Oscillations for Earth Tomography*, *Nucl. Phys. B* **908** (2016) 250–267, [[arXiv:1511.05154](https://arxiv.org/abs/1511.05154)].
- [44] R. Gandhi, C. Quigg, M. H. Reno, and I. Sarcevic, *Ultra-high-energy neutrino interactions*, *Astropart. Phys.* **5** (1996) 81–110, [[hep-ph/9512364](https://arxiv.org/abs/hep-ph/9512364)].
- [45] **IceCube** Collaboration, M. G. Aartsen et al., *Measurement of the multi-TeV neutrino cross section with IceCube using Earth absorption*, *Nature* **551** (2017) 596–600, [[arXiv:1711.08119](https://arxiv.org/abs/1711.08119)].

- [46] A. Placci and E. Zavattini, *On the possibility of using high-energy neutrinos to study the earth's interior*, tech. rep., CERN, Geneva, Oct, 1973.
- [47] L. V. Volkova and G. T. Zatsepin, *On the problem of neutrino penetration through the earth. (talk, in russian)*, *Izv. Akad. Nauk Ser. Fiz.* **38N5** (1974) 1060–1063.
- [48] I. Nedyalkov, *Notes on neutrino tomography*, *Acad. Bulgarian Sci.* **34** (1981) 177–180.
- [49] I. Nedyalkov, *On the study of the Earth structure by neutrino experiments*, tech. rep., Joint Inst. for Nuclear Research, Dubna (USSR). Lab. of Nuclear Problems, USSR, 1981. JINR-R-2-81-645.
- [50] I. Nedyalkov, *On the study of the Earth composition by means of neutrino experiments, Balatonfuered 1982*, *Proc. Neutrino '82* **1** (1981) 300.
- [51] I. P. Nedialkov, *Measurement of projected mass density - a basic problem of neutrino geophysics*, *Bolgarska Akademiia Nauk Doklady* **36** (Jan., 1983) 1515–1518.
- [52] A. Krastev and J. Nedialkov, *A numerical solution of the equation of the computerized tomography and its application in astrophysics*, tech. rep., Joint Inst. for Nuclear Research, Dubna (USSR). Lab. of Computing Techniques and Automation, USSR, 1983. JINR-E-11-83-692.
- [53] A. De Rujula, S. L. Glashow, R. R. Wilson, and G. Charpak, *Neutrino Exploration of the Earth*, *Phys. Rept.* **99** (1983) 341.
- [54] T. L. Wilson, *Neutrino Tomography: Tevatron Mapping Versus the Neutrino Sky*, *Nature* **309** (1984) 38–42.
- [55] G. A. Askarian, *Investigation of the Earth by means of neutrinos. Neutrino geology*, *Sov. Phys. Usp.* **27** (1984) 896–990.
- [56] L. V. Volkova, *Neutrino Detection at Large Distances from Accelerators*, *Nuovo Cim. C* **8** (1985) 552–578.
- [57] V. A. Tsarev, *Geophysical applications of neutrino beams*, *Sov. Phys. Usp.* **28** (1985) 940.
- [58] A. B. Borisov, B. A. Dolgoshein, and A. N. Kalinovsky, *Direct Method for Determination of Differential Distribution of the Earth Density by Means of High-energy Neutrino Scattering. (In Russian)*, *Yad. Fiz.* **44** (1986) 681–689.
- [59] V. A. Tsarev and V. A. Chechin, *Long Distance Neutrino. Physical Principles and Geophysical Applications. (In Russian)*, *Fiz. Elem. Chast. Atom. Yadra* **17** (1986) 389–432.
- [60] A. B. Borisov and B. A. Dolgoshein, *Determination of rock density by means of high-energy neutrino beams by the delayed muon method*, *Phys. Atom. Nucl.* **56** (1993) 755–761.
- [61] C. Kuo, H. J. Crawford, R. Jeanloz, B. Romanowicz, G. Shapiro, and M. L. Stevenson, *Extraterrestrial neutrinos and Earth Structure*, *Earth and Planet Science Lett.* (1995) 95–103.
- [62] **DUMAND** Collaboration, H. J. Crawford, R. Jeanloz, and B. Romanowicz, *Mapping the earth's interior with astrophysical neutrinos*, in *International Cosmic Ray Conference*, vol. 1, p. 804, Dumand Collaboration, Jan., 1995.
- [63] P. Jain, J. P. Ralston, and G. M. Frichter, *Neutrino absorption tomography of the earth's interior using isotropic ultrahigh-energy flux*, *Astropart. Phys.* **12** (1999) 193–198, [[hep-ph/9902206](https://arxiv.org/abs/hep-ph/9902206)].

- [64] M. M. Reynoso and O. A. Sampayo, *On neutrino absorption tomography of the earth*, *Astropart. Phys.* **21** (2004) 315–324, [[hep-ph/0401102](#)].
- [65] E. Borriello, G. Mangano, A. Marotta, G. Miele, P. Migliozzi, C. A. Moura, S. Pastor, O. Pisanti, and P. E. Strolin, *Sensitivity on Earth Core and Mantle densities using Atmospheric Neutrinos*, *JCAP* **06** (2009) 030, [[arXiv:0904.0796](#)].
- [66] N. Takeuchi, *Simulation of heterogeneity sections obtained by neutrino radiography*, *Earth, Planets and Space* **62** (Feb., 2010) 215–221.
- [67] I. Romero and O. A. Sampayo, *About the Earth density and the neutrino interaction*, *Eur. Phys. J. C* **71** (2011) 1696.
- [68] F. Capozzi, E. Di Valentino, E. Lisi, A. Marrone, A. Melchiorri, and A. Palazzo, *Unfinished fabric of the three neutrino paradigm*, *Phys. Rev. D* **104** (2021), no. 8 083031, [[arXiv:2107.00532](#)].
- [69] NuFIT v5.2 (2022), <http://www.nu-fit.org/>.
- [70] I. Esteban, M. C. Gonzalez-Garcia, M. Maltoni, T. Schwetz, and A. Zhou, *The fate of hints: updated global analysis of three-flavor neutrino oscillations*, *JHEP* **09** (2020) 178, [[arXiv:2007.14792](#)].
- [71] P. F. de Salas, D. V. Forero, S. Gariazzo, P. Martínez-Miravé, O. Mena, C. A. Ternes, M. Tórtola, and J. W. F. Valle, *2020 global reassessment of the neutrino oscillation picture*, *JHEP* **02** (2021) 071, [[arXiv:2006.11237](#)].
- [72] V. K. Ermilova, V. A. Tsarev, and V. A. Chechin, *Buildup of Neutrino Oscillations in the Earth*, *JETP Lett.* **43** (1986) 453–456.
- [73] A. Nicolaidis, *Neutrinos for Geophysics*, *Phys. Lett. B* **200** (1988) 553–559.
- [74] V. Ermilova, V. Tsarev, and V. Chechin, *Restoration of the Density Distribution of Material Based on Neutrino Oscillations*, *Bull. Lebedev Phys. Inst.* **1988N3** (1988) 51–54.
- [75] A. Nicolaidis, M. Jannane, and A. Tarantola, *Neutrino tomography of the earth*, *J. Geophys. Res.* **96** (1991), no. B13 21811–21817.
- [76] T. Ohlsson and W. Winter, *Reconstruction of the earth’s matter density profile using a single neutrino baseline*, *Phys. Lett. B* **512** (2001) 357–364, [[hep-ph/0105293](#)].
- [77] T. Ohlsson and W. Winter, *Could one find petroleum using neutrino oscillations in matter?*, *Europhys. Lett.* **60** (2002) 34–39, [[hep-ph/0111247](#)].
- [78] W. Winter, *Probing the absolute density of the Earth’s core using a vertical neutrino beam*, *Phys. Rev. D* **72** (2005) 037302, [[hep-ph/0502097](#)].
- [79] H. Minakata and S. Uchinami, *On in situ Determination of Earth Matter Density in Neutrino Factory*, *Phys. Rev. D* **75** (2007) 073013, [[hep-ph/0612002](#)].
- [80] R. Gandhi and W. Winter, *Physics with a very long neutrino factory baseline*, *Phys. Rev. D* **75** (2007) 053002, [[hep-ph/0612158](#)].
- [81] J. Tang and W. Winter, *Requirements for a New Detector at the South Pole Receiving an Accelerator Neutrino Beam*, *JHEP* **02** (2012) 028, [[arXiv:1110.5908](#)].
- [82] C. A. Argüelles, M. Bustamante, and A. M. Gago, *Searching for cavities of various densities in the Earth’s crust with a low-energy  $\bar{\nu}_e$   $\beta$ -beam*, *Mod. Phys. Lett. A* **30** (2015), no. 29 1550146, [[arXiv:1201.6080](#)].

- [83] A. N. Ioannisian and A. Y. Smirnov, *Matter effects of thin layers: Detecting oil by oscillations of solar neutrinos*, 1, 2002.
- [84] A. N. Ioannisian and A. Y. Smirnov, *Neutrino oscillations in low density medium*, *Phys. Rev. Lett.* **93** (2004) 241801, [[hep-ph/0404060](#)].
- [85] E. K. Akhmedov, M. A. Tortola, and J. W. F. Valle, *Geotomography with solar and supernova neutrinos*, *JHEP* **06** (2005) 053, [[hep-ph/0502154](#)].
- [86] A. N. Ioannisian, A. Y. Smirnov, and D. Wyler, *Oscillations of the  ${}^7\text{Be}$  solar neutrinos inside the Earth*, *Phys. Rev. D* **92** (2015), no. 1 013014, [[arXiv:1503.02183](#)].
- [87] A. N. Ioannisian and A. Y. Smirnov, *Attenuation effect and neutrino oscillation tomography*, *Phys. Rev. D* **96** (2017), no. 8 083009, [[arXiv:1705.04252](#)].
- [88] A. Ioannisian, A. Smirnov, and D. Wyler, *Scanning the Earth with solar neutrinos and DUNE*, *Phys. Rev. D* **96** (2017), no. 3 036005, [[arXiv:1702.06097](#)].
- [89] P. Bakhti and A. Y. Smirnov, *Oscillation tomography of the Earth with solar neutrinos and future experiments*, *Phys. Rev. D* **101** (2020), no. 12 123031, [[arXiv:2001.08030](#)].
- [90] M. Lindner, T. Ohlsson, R. Tomas, and W. Winter, *Tomography of the earth's core using supernova neutrinos*, *Astropart. Phys.* **19** (2003) 755–770, [[hep-ph/0207238](#)].
- [91] R. Hajjar, O. Mena, and S. Palomares-Ruiz, *Earth tomography with supernova neutrinos at future neutrino detectors*, *Phys. Rev. D* **108** (2023), no. 8 083011, [[arXiv:2303.09369](#)].
- [92] S. K. Agarwalla, T. Li, O. Mena, and S. Palomares-Ruiz, *Exploring the Earth matter effect with atmospheric neutrinos in ice*, 12, 2012.
- [93] **IceCube-PINGU** Collaboration, M. G. Aartsen et al., *Letter of Intent: The Precision IceCube Next Generation Upgrade (PINGU)*, 1, 2014.
- [94] C. Rott, A. Taketa, and D. Bose, *Spectrometry of the Earth using Neutrino Oscillations*, *Sci. Rep.* **5** (2015) 15225, [[arXiv:1502.04930](#)].
- [95] **KM3NeT** Collaboration, S. Bourret, J. a. A. B. Coelho, and V. Van Elewyck, *Neutrino oscillation tomography of the Earth with KM3NeT-ORCA*, *J. Phys. Conf. Ser.* **888** (2017), no. 1 012114, [[arXiv:1702.03723](#)].
- [96] **KM3NeT** Collaboration, S. Bourret and V. Van Elewyck, *Earth tomography with neutrinos in KM3NeT-ORCA*, *EPJ Web Conf.* **207** (2019) 04008.
- [97] S. Bourret, J. Coelho, E. Kaminski, and V. Van Elewyck, *Probing the Earth Core Composition with Neutrino Oscillation Tomography*, *PoS ICRC2019* (2020) 1024.
- [98] J. C. D'Olivo, J. A. Herrera Lara, I. Romero, O. A. Sampayo, and G. Zapata, *Earth tomography with atmospheric neutrino oscillations*, *Eur. Phys. J. C* **80** (2020), no. 10 1001.
- [99] A. Kumar and S. K. Agarwalla, *Validating the Earth's core using atmospheric neutrinos with ICAL at INO*, *JHEP* **08** (2021) 139, [[arXiv:2104.11740](#)].
- [100] **KM3NeT** Collaboration, L. Maderer, J. Coelho, E. Kaminski, and V. Van Elewyck, *KM3NeT performance on oscillation and absorption tomography of the Earth*, *PoS ICRC2021* (2021) 1172.
- [101] P. B. Denton and R. Pestes, *Neutrino oscillations through the Earth's core*, *Phys. Rev. D* **104** (10, 2021) 113007, [[arXiv:2110.01148](#)].

- [102] K. J. Kelly, P. A. N. Machado, I. Martinez-Soler, and Y. F. Perez-Gonzalez, *DUNE atmospheric neutrinos: Earth tomography*, *JHEP* **05** (2022) 187, [[arXiv:2110.00003](#)].
- [103] F. Capozzi and S. T. Petcov, *Neutrino tomography of the Earth with ORCA detector*, *Eur. Phys. J. C* **82** (2022), no. 5 461, [[arXiv:2111.13048](#)].
- [104] J. C. D’Olivo Saez, J. A. H. Lara, I. Romero, and O. A. Sampayo, *Oscillation tomography study of Earth’s composition and density with atmospheric neutrinos*, *Eur. Phys. J. C* **82** (2022), no. 7 614, [[arXiv:2207.11257](#)].
- [105] L. Maderer, E. Kaminski, J. A. B. Coelho, S. Bourret, and V. Van Elewyck, *Unveiling the outer core composition with neutrino oscillation tomography*, *Front. Earth Sci.* **11** (2023) 1008396, [[arXiv:2208.00532](#)].
- [106] A. K. Upadhyay, A. Kumar, S. K. Agarwalla, and A. Dighe, *Locating the core-mantle boundary using oscillations of atmospheric neutrinos*, *JHEP* **04** (2023) 068, [[arXiv:2211.08688](#)].
- [107] A. K. Upadhyay, A. Kumar, S. K. Agarwalla, and A. Dighe, *Probing dark matter inside Earth using atmospheric neutrino oscillations at INO-ICAL*, *Phys. Rev. D* **107** (2023), no. 11 115030, [[arXiv:2112.14201](#)].
- [108] L. Wolfenstein, *Neutrino Oscillations in Matter*, *Phys. Rev. D* **17** (1978) 2369–2374.
- [109] S. P. Mikheev and A. Y. Smirnov, *Resonance enhancement of oscillations in matter and solar neutrino spectroscopy*, *Sov. J. Nucl. Phys.* **42** (1985) 913. [*Yad.Fiz.*42:1441-1448,1985].
- [110] S. P. Mikheev and A. Y. Smirnov, *Resonant amplification of neutrino oscillations in matter and solar neutrino spectroscopy*, *Nuovo Cim. C* **9** (1986) 17–26.
- [111] S. Petcov, *Diffraction-like (or parametric resonance-like?) enhancement of the earth (day - night) effect for solar neutrinos crossing the earth core*, *Phys. Lett. B* **434** (1998) 321, [[hep-ph/9805262](#)].
- [112] M. Chizhov, M. Maris, and S. T. Petcov, *On the oscillation length resonance in the transitions of solar and atmospheric neutrinos crossing the earth core*, 7, 1998.
- [113] S. T. Petcov, *New enhancement mechanism of the transitions in the earth of the solar and atmospheric neutrinos crossing the earth core*, *Nucl. Phys. B Proc. Suppl.* **77** (1999) 93–97, [[hep-ph/9809587](#)].
- [114] M. Chizhov and S. Petcov, *New conditions for a total neutrino conversion in a medium*, *Phys.Rev.Lett.* **83** (1999) 1096–1099, [[hep-ph/9903399](#)].
- [115] M. V. Chizhov and S. T. Petcov, *Enhancing mechanisms of neutrino transitions in a medium of nonperiodic constant density layers and in the earth*, *Phys. Rev. D* **63** (2001) 073003, [[hep-ph/9903424](#)].
- [116] E. K. Akhmedov, *Parametric resonance of neutrino oscillations and passage of solar and atmospheric neutrinos through the earth*, *Nucl. Phys. B* **538** (1999) 25–51, [[hep-ph/9805272](#)].
- [117] E. K. Akhmedov, A. Dighe, P. Lipari, and A. Y. Smirnov, *Atmospheric neutrinos at Super-Kamiokande and parametric resonance in neutrino oscillations*, *Nucl. Phys. B* **542** (1999) 3–30, [[hep-ph/9808270](#)].
- [118] **IceCube** Collaboration, M. G. Aartsen et al., *The IceCube Neutrino Observatory*:

- Instrumentation and Online Systems, JINST* **12** (2017), no. 03 P03012, [[arXiv:1612.05093](https://arxiv.org/abs/1612.05093)].
- [119] **IceCube** Collaboration, R. Abbasi et al., *The Design and Performance of IceCube DeepCore*, *Astropart. Phys.* **35** (2012) 615–624, [[arXiv:1109.6096](https://arxiv.org/abs/1109.6096)].
- [120] **KM3Net** Collaboration, S. Adrian-Martinez et al., *Letter of intent for KM3NeT 2.0*, *J. Phys. G* **43** (2016), no. 8 084001, [[arXiv:1601.07459](https://arxiv.org/abs/1601.07459)].
- [121] **DUNE** Collaboration, A. Abed Abud et al., *Deep Underground Neutrino Experiment (DUNE) Near Detector Conceptual Design Report*, *Instruments* **5** (2021), no. 4 31, [[arXiv:2103.13910](https://arxiv.org/abs/2103.13910)].
- [122] **Hyper-Kamiokande** Collaboration, K. Abe et al., *Hyper-Kamiokande Design Report*, 5, 2018.
- [123] **ICAL** Collaboration, S. Ahmed et al., *Physics Potential of the ICAL detector at the India-based Neutrino Observatory (INO)*, *Pramana* **88** (2017), no. 5 79, [[arXiv:1505.07380](https://arxiv.org/abs/1505.07380)].
- [124] A. Kumar, *Probing interiors of earth using magnetized neutrino detector*, 2023. Talk given at the International Workshop on Multi-messenger Tomography of the Earth (MMTE 2023), APC, Paris, France, [https://indico.in2p3.fr/event/30001/contributions/126613/attachments/79006/115411/MMTE\\_2023\\_ICAL\\_INO\\_Anil\\_Kumar.pdf](https://indico.in2p3.fr/event/30001/contributions/126613/attachments/79006/115411/MMTE_2023_ICAL_INO_Anil_Kumar.pdf).
- [125] A. K. Upadhyay, *Probing the properties of core-mantle boundary using atmospheric neutrino oscillation*, 2023. Talk given at the International Workshop on Multi-messenger Tomography of the Earth (MMTE 2023), APC, Paris, France, [https://indico.in2p3.fr/event/30001/contributions/126325/attachments/79009/115407/MMTE2023\\_talk\\_Anuj\\_Upadhyay.pdf](https://indico.in2p3.fr/event/30001/contributions/126325/attachments/79009/115407/MMTE2023_talk_Anuj_Upadhyay.pdf).
- [126] S. K. Agarwalla, *Probing the interior of earth using neutrino oscillations in icecube-deepcore*, 2023. Talk given at the International Workshop on Multi-messenger Tomography of the Earth (MMTE 2023), APC, Paris, France, [https://indico.in2p3.fr/event/30001/contributions/126089/attachments/78952/115321/Interior-Earth-IceCube-DeepCore\\_v3.pdf](https://indico.in2p3.fr/event/30001/contributions/126089/attachments/78952/115321/Interior-Earth-IceCube-DeepCore_v3.pdf).
- [127] N. Song, S. W. Li, C. A. Argüelles, M. Bustamante, and A. C. Vincent, *The Future of High-Energy Astrophysical Neutrino Flavor Measurements*, *JCAP* **04** (2021) 054, [[arXiv:2012.12893](https://arxiv.org/abs/2012.12893)].
- [128] A. Kumar, A. Khatun, S. K. Agarwalla, and A. Dighe, *From oscillation dip to oscillation valley in atmospheric neutrino experiments*, *Eur. Phys. J. C* **81** (2021), no. 2 190, [[arXiv:2006.14529](https://arxiv.org/abs/2006.14529)].
- [129] A. Kumar, A. Khatun, S. K. Agarwalla, and A. Dighe, *A New Approach to Probe Non-Standard Interactions in Atmospheric Neutrino Experiments*, *JHEP* **04** (2021) 159, [[arXiv:2101.02607](https://arxiv.org/abs/2101.02607)].
- [130] S. P. Behera, M. S. Bhatia, V. M. Datar, and A. K. Mohanty, *Simulation Studies for Electromagnetic Design of INO ICAL Magnet and its Response to Muons*, *IEEE Trans. Magnetics* **51** (2015) 4624, [[arXiv:1406.3965](https://arxiv.org/abs/1406.3965)].
- [131] N. Dash, V. M. Datar, and G. Majumder, *A Study on the time resolution of Glass RPC*, 10, 2014.

- [132] A. D. Bhatt, V. M. Datar, G. Majumder, N. K. Mondal, P. Pathaleswar, and B. Satyanarayana, *Improvement of time measurement with the INO-ICAL resistive plate chambers*, *JINST* **11** (2016), no. 11 C11001.
- [133] A. Gaur, A. Kumar, and M. Naimuddin, *Study of timing response and charge spectra of glass based Resistive Plate Chamber detectors for INO-ICAL experiment*, *JINST* **12** (2017), no. 03 C03081.
- [134] A. Chatterjee, K. K. Meghna, K. Rawat, T. Thakore, V. Bhatnagar, R. Gandhi, D. Indumathi, N. K. Mondal, and N. Sinha, *A Simulations Study of the Muon Response of the Iron Calorimeter Detector at the India-based Neutrino Observatory*, *JINST* **9** (2014) P07001, [[arXiv:1405.7243](#)].
- [135] M. M. Devi, A. Ghosh, D. Kaur, L. S. Mohan, S. Choubey, A. Dighe, D. Indumathi, S. Kumar, M. V. N. Murthy, and M. Naimuddin, *Hadron energy response of the Iron Calorimeter detector at the India-based Neutrino Observatory*, *JINST* **8** (2013) P11003, [[arXiv:1304.5115](#)].
- [136] D. Casper, *The Nuance neutrino physics simulation, and the future*, *Nucl. Phys. B Proc. Suppl.* **112** (2002) 161–170, [[hep-ph/0208030](#)].
- [137] M. Sajjad Athar, M. Honda, T. Kajita, K. Kasahara, and S. Midorikawa, *Atmospheric neutrino flux at INO, South Pole and Pyh asalmi*, *Phys. Lett.* **B718** (2013) 1375, [[arXiv:1210.5154](#)].
- [138] M. Honda, M. Sajjad Athar, T. Kajita, K. Kasahara, and S. Midorikawa, *Atmospheric neutrino flux calculation using the NRLMSISE-00 atmospheric model*, *Phys. Rev. D* **92** (2015), no. 2 023004, [[arXiv:1502.03916](#)].
- [139] N. Dash, *Feasibility studies for the detection of exotic particles using ICAL at INO*. PhD thesis, HBNI, Mumbai, 2015.
- [140] M. M. Devi, T. Thakore, S. K. Agarwalla, and A. Dighe, *Enhancing sensitivity to neutrino parameters at INO combining muon and hadron information*, *JHEP* **10** (2014) 189, [[arXiv:1406.3689](#)].
- [141] A. Ghosh, T. Thakore, and S. Choubey, *Determining the Neutrino Mass Hierarchy with INO, T2K, NOvA and Reactor Experiments*, *JHEP* **04** (2013) 009, [[arXiv:1212.1305](#)].
- [142] T. Thakore, A. Ghosh, S. Choubey, and A. Dighe, *The Reach of INO for Atmospheric Neutrino Oscillation Parameters*, *JHEP* **05** (2013) 058, [[arXiv:1303.2534](#)].
- [143] M. Blennow, P. Coloma, P. Huber, and T. Schwetz, *Quantifying the sensitivity of oscillation experiments to the neutrino mass ordering*, *JHEP* **03** (2014) 028, [[arXiv:1311.1822](#)].
- [144] S. Baker and R. D. Cousins, *Clarification of the Use of Chi Square and Likelihood Functions in Fits to Histograms*, *Nucl. Instrum. Meth.* **221** (1984) 437–442.
- [145] M. C. Gonzalez-Garcia and M. Maltoni, *Atmospheric neutrino oscillations and new physics*, *Phys. Rev. D* **70** (2004) 033010, [[hep-ph/0404085](#)].
- [146] P. Huber, M. Lindner, and W. Winter, *Superbeams versus neutrino factories*, *Nucl. Phys. B* **645** (2002) 3–48, [[hep-ph/0204352](#)].
- [147] G. L. Fogli, E. Lisi, A. Marrone, D. Montanino, and A. Palazzo, *Getting the most from the statistical analysis of solar neutrino oscillations*, *Phys. Rev. D* **66** (2002) 053010, [[hep-ph/0206162](#)].

- [148] E. K. Akhmedov, R. Johansson, M. Lindner, T. Ohlsson, and T. Schwetz, *Series expansions for three flavor neutrino oscillation probabilities in matter*, *JHEP* **04** (2004) 078, [[hep-ph/0402175](#)].